Investigation of Imaging Capabilities for Dual Cone-Beam Computed Tomography

by

Hao Li

Graduate Program in Medical Physics
Duke University

Date:___________________________
Approved:

____
Fang-Fang Yin, Supervisor

____
James Bowsher

____
James Colsher

____
James T Dobbins III

____
Qingrong Jackie Wu

Dissertation submitted in partial fulfillment of
the requirements for the degree of Doctor of Philosophy
in the Graduate Program in Medical Physics
in the Graduate School
of Duke University

2013

ABSTRACT

Investigation of Imaging Capabilities for Dual Cone-Beam Computed Tomography

by

Hao Li

Graduate Program in Medical Physics
Duke University

Date:____________________________
Approved:

____
Fang-Fang Yin, Supervisor

____
James Bowsher

____
James Colsher

____
James T Dobbins III

____
Qingrong Jackie Wu

An abstract of a dissertation submitted in partial fulfillment of
the requirements for the degree of Doctor of Philosophy
in the Graduate Program in Medical Physics
in the Graduate School
of Duke University

2013

Abstract

A bench-top dual cone-beam computed tomography (CBCT) system was developed consisting of two orthogonally placed 40x30 cm^2 flat-panel detectors and two conventional X-ray tubes with two individual high-voltage generators sharing the same rotational axis. The X-ray source to detector distance is 150 cm and X-ray source to rotational axis distance is 100 cm for both subsystems. The objects are scanned through 200° of rotation. The dual CBCT (DCBCT) system utilized 110° of projection data from one detector and 90° from the other while the two individual single CBCTs utilized 200° data from each detector. The system performance was characterized in terms of uniformity, contrast, spatial resolution, noise power spectrum and CT number linearity. The uniformity, within the axial slice and along the longitudinal direction, and noise power spectrum were assessed by scanning a water bucket; the contrast and CT number linearity were measured using the Catphan phantom; and the spatial resolution was evaluated using a tungsten wire phantom. A skull phantom and a ham were also scanned to provide qualitative evaluation of high- and low-contrast resolution. Each measurement was compared between dual and single CBCT systems.

Compared with single CBCT, the DCBCT presented: 1) a decrease in uniformity by 1.9% in axial view and 1.1% in the longitudinal view, as averaged for four energies (80, 100, 125 and 150 kVp); 2) comparable or slightly better contrast to noise ratio (CNR) for low-contrast objects and comparable contrast for high-contrast objects; 3) comparable

spatial resolution; 4) comparable CT number linearity with $R^2 \geq 0.99$ for all four tested energies; 5) lower noise power spectrum in magnitude. DCBCT images of the skull phantom and the ham demonstrated both high-contrast resolution and good soft-tissue contrast.

One of the major challenges for clinical implementation of four-dimensional (4D) CBCT is the long scan time. To investigate the 4D imaging capabilities of the DCBCT system, motion phantom studies were conducted to validate the efficiency by comparing 4D images generated from 4D-DCBCT and 4D-CBCT. First, a simple sinusoidal profile was used to confirm the scan time reduction. Next, both irregular sinusoidal and patient-derived profiles were used to investigate the advantage of temporally correlated orthogonal projections due to a reduced scan time. Normalized mutual information (NMI) between 4D-DCBCT and 4D-CBCT was used for quantitative evaluation.

For the simple sinusoidal profile, the average NMI for ten phases between two single 4D-CBCTs was 0.336, indicating the maximum NMI that can be achieved for this study. The average NMIs between 4D-DCBCT and each single 4D-CBCT were 0.331 and 0.320. For both irregular sinusoidal and patient-derived profiles, 4D-DCBCT generated phase images with less motion blurring when compared with single 4D-CBCT.

For dual kV energy imaging, we acquired 80kVp projections and 150 kVp projections, with an additional 0.8 mm tin filtration. The virtual monochromatic (VM) technique was implemented, by first decomposing these projections into acrylic and

aluminum basis material projections to synthesize VM projections, which were then used to reconstruct VM CBCTs. The effect of the VM CBCT on metal artifact reduction was evaluated with an in-house titanium-BB phantom. The optimal VM energy to maximize CNR for iodine contrast and minimize beam hardening in VM CBCT was determined using a water phantom containing two iodine concentrations. The linearly-mixed (LM) technique was implemented by linearly combining the low- (80kVp) and high-energy (150kVp) CBCTs. The dose partitioning between low- and high-energy CBCTs was varied (20%, 40%, 60% and 80% for low-energy) while keeping total dose approximately equal to single-energy CBCTs, measured using an ion chamber. Noise levels and CNRs for four tissue types were investigated for dual-energy LM CBCTs in comparison with single-energy CBCTs at 80, 100, 125 and 150kVp.

The VM technique showed a substantial reduction of metal artifacts at 100 keV with a 40% reduction in the background standard deviation compared with a 125 kVp single-energy scan of equal dose. The VM energy to maximize CNR for both iodine concentrations and minimize beam hardening in the metal-free object was 50 keV and 60 keV, respectively. The difference in average noise levels measured in the phantom background was 1.2% for dual-energy LM CBCTs and equivalent-dose single-energy CBCTs. CNR values in the LM CBCTs of any dose partitioning were better than those of 150 kVp single-energy CBCTs. The average CNRs for four tissue types with 80% dose fraction at low-energy showed 9.0% and 4.1% improvement relative to 100 kVp and 125

kVp single-energy CBCTs, respectively. CNRs for low contrast objects improved as dose partitioning was more heavily weighted towards low-energy (80kVp) for LM CBCTs.

For application of the dual-energy technique in the kilovoltage (kV) and megavoltage (MV) range, we acquired both MV projections (from gantry angle of 0° to 100°) and kV projections (90° to 200°) with the current orthogonal kV/MV imaging hardware equipped in modern linear accelerators, as gantry rotated a total of 110°. A selected range of overlap projections between 90° to 100° were then decomposed into two material projections using experimentally determined parameters from orthogonally stacked aluminum and acrylic step-wedges. Given attenuation coefficients of aluminum and acrylic at a predetermined energy, one set of VM projections could be synthesized from two corresponding sets of decomposed projections. Two linear functions were generated using projection information at overlap angles to convert kV and MV projections at non-overlap angles to approximate VM projections for CBCT reconstruction. The CNRs were calculated for different inserts in VM CBCTs of a CatPhan phantom with various selected energies and compared with those in kV and MV CBCTs. The effect of overlap projection number on CNR was evaluated. Additionally, the effect of beam orientation was studied by scanning the CatPhan sandwiched with two 5 cm solid-water phantoms on both lateral sides and an electronic density phantom with two metal bolt inserts.

Proper selection of VM energy (30keV and 40keV for low-density polyethylene (LDPE), polymethylpentene (PMP), 2MeV for Delrin) provided comparable or even better CNR results as compared with kV or MV CBCT. An increased number of overlap between kV and MV projections demonstrated only marginal improvements of CNR for different inserts (with the exception of LDPE) and therefore one projection overlap was found to be sufficient for the CatPhan study. It was also evident that the optimal CBCT image quality was achieved when MV beams penetrated through the heavy attenuation direction of the object.

In conclusion, the performance of a bench-top DCBCT imaging system has been characterized and is comparable to that of a single CBCT. The 4D-DCBCT provides an efficient 4D imaging technique for motion management. The scan time is reduced by approximately a factor of two. The temporally correlated orthogonal projections improved the image blur across 4D phase images. Dual-energy CBCT imaging techniques were implemented to synthesize VM CBCT and LM CBCTs. VM CBCT was effective at achieving metal artifact reduction. Depending on the dose-partitioning scheme, LM CBCT demonstrated the potential to improve CNR for low contrast objects compared with single-energy CBCT acquired with equivalent dose. A novel technique was developed to generate VM CBCTs from kV/MV projections. This technique has the potential to improve CNR at selected VM energies and to suppress artifacts at appropriate beam orientations.

Contents

List of Tables

List of Figures

List of Abbreviations

2D	two-dimensional
3D	three-dimensional
4D	four-dimensional
AOR	axis of rotation
CBCT	cone-beam computed tomography
CNR	contrast-to-noise ratio
CT	computed tomography
DCBCT	dual cone-beam computed tomography
DTS	digital tomosynthesis
FDK	Feldkamp Davis Kress reconstruction algorithm
FOV	field of view
HU	Hounsfield unit
IGRT	image guided radiation therapy
IMRT	intensity modulated radiation therapy
kV	kilovoltage
kVp	peak kilovoltage
LDPE	Low density polyethylene
LINAC	linear accelerator
LM	linearly mixed

MTF	modulation transfer function
MV	megavoltage
NPS	noise power spectrum
OBI	On-Board Imager
PS	Polystyrene
PSF	point spread function
PMP	Polymethylpentene
ROI	region of interest
SAD	source to axis distance
SART	simultaneous algebraic reconstruction techniques
SID	source to imager distance
VM	virtual monochromatic
XML	extensible markup language

Acknowledgements

Firstly, I am deeply indebted to my supervisor, Dr. Fang-Fang Yin, who has been an extremely supportive and caring mentor and continued to challenge me to be a more thoughtful scientist. Dr. Yin has always helped me tremendously from the beginning to the end of my project, offered me thorough reviews of my work and provided abundant practical aspects of clinical radiation therapy.

I am also deeply indebted to other professors on my PhD committee. I thank Dr. James Bowsher for his insightful questions on my research, and patient and tireless discussions on my publications. I also thank Dr. James Colsher for teaching me to look at the big picture about research in the medical physics field. I am also grateful to Dr. James T Dobbins III for never ceasing to ask detailed questions and showing me the importance of leadership in medical physics. My deep appreciation is also due to Dr. Qingrong Jackie Wu for her valuable clinical insights.

I am grateful for the financial support from Varian Medical Systems and Medical Physics Graduate Program at Duke University. I also greatly appreciate the help received from many other mentors, colleagues and friends at Duke University. I would like to thank Dr. William Giles for his collaboration on the dual cone-beam CT system. I thank Dr. Devon Godfrey for his help and discussion on the imaging system characterization. I thank Dr. Irina Vergalasova who has been kind enough to read through drafts of my papers and Dr. Taoran Li for his comments on various research topics, and for them sharing the office with me for the past four years. I also thank Anna Rodrigues for her editing support on my dissertation.

Finally, and most importantly, I dedicate this dissertation to my parents, Dezheng Li and Lan Ding, from whom I have received unwavering support and encouragement.

1. Introduction

1.1 General Introduction

1.1.1 Clinical motivation

Cancer is the second leading cause of death behind heart disease in the United States. A total of approximately 1.66 million new cancer cases and 580,000 cancer deaths are projected to occur in the United States in 2013[1].

High-energy radiation has been widely adopted for cancer treatment. The radiation may be delivered from outside the body (external-beam), e.g. linear accelerator (LINAC), or from radioactive material placed inside the body, e.g. brachytherapy. The high-energy radiation kills cancer cells by damaging their DNA. However, radiation therapy can damage normal cells as well as cancer cells. Therefore, one goal in radiation therapy treatment planning is to simultaneously deliver tumoricidal dose to cancer cells and spare nearby healthy tissue.

During the past few decades, radiation therapy has undergone several innovations. It is now possible to deliver highly conformal radiation dose with steep dose gradients in the tumor region using techniques such as intensity modulated radiation therapy (IMRT). Internal organ motion exists during each treatment fraction and displacement can happen between fractions. With the improved dose distribution, it is therefore necessary to warrant the reproducibility of beam delivery during treatment and between fractions. Tumor localization is critical to achieve this goal, especially in the external-beam treatment. In recent years, image-guided radiation therapy (IGRT) has been utilized to minimize these uncertainties during beam delivery[2-5]. The broad definition of IGRT means application of imaging, image analysis, and intervention techniques at each step of radiation therapy. Specifically, IGRT here refers to the application of imaging in the process of radiation therapy, mainly in the treatment room. During the early days of radiation therapy, kilovoltage (kV) radiographs were used by radiation oncologists for tumor localization. The invention of CT in the 1970s revolutionized radiation therapy and allowed for three-dimensional conformal delivery. Installation of a kV source and flat-panel detectors on the LINAC offers on-board cone-beam CT (CBCT) capabilities during the treatment and has gradually become a standard in most clinics.

1.1.2 Dual Cone-Beam CT

Since its inception, CBCT with a kV source has been widely adopted for image-guidance in the treatment room to improve the accuracy of target localization, as it can be integrated on a LINAC. While kV CBCT provides high spatial resolution, improved soft tissue contrast when compared with 2D radiography, and volumetric acquisition[2, 6-9], CBCT still experiences a number of challenges. One complete CBCT acquisition using an on-board imager still takes about one minute, which renders a breath-hold CT scan difficult to implement[10].

Adding another set of X-ray source/detector orthogonally may provide many additional imaging capabilities and this has already been implemented for the clinical CT[11]. Using two orthogonally placed sets of kV X-ray source/detectors may reduce the total scan time required compared with the current single CBCT systems, and it would have potential to provide dual-energy imaging for material differentiation and artifact reduction[11-13]. A dual cone-beam on-board imaging device would also allow for simultaneous and orthogonal radiographs[14], which have been shown to be highly useful in similar systems for target localization.

To investigate the potential advantages of the dual-kV CBCT, we thus have built a prototype dual CBCT (DCBCT) system (as shown in Figure 1-1(a)) consisted of two X-ray tubes (Varian G-242, Varian Medical Systems, Palo Alto, CA) and two large flat-panel detectors (PaxScan® 4030CB, Varian Medical Systems, Palo Alto, CA) together with a rotational stage in the middle for imaging objects. These components were mounted on an optical bench with an angular separation of 90° between the two single CBCT systems. The X-rays tubes were powered by two CPI Indico 100 RF 50kW generators (Communications & Power Industries, Palo Alto, CA) and had an equivalent 0.7 mm aluminum filtration at the exit window. The collimator box for each X-ray tube consisted of two sets of adjustable blades along the horizontal and vertical directions and had an equivalent 2 mm aluminum filtration as specified by the manufacturer. Each flat-panel detector had a pixel area of 397x298 mm^2 and a pixel pitch of 194 μm. The detector allows different pixel binning modes and a maximal readout frame rate of 30 frames per second. The anti-scatter grid provided by the manufacturer was also mounted on the system to minimize scattered photons from the corresponding and orthogonal X-ray sources. The focus of the work is to characterize the imaging performance of the DCBCT system for advanced imaging tasks. Specifically, the system performance was characterized in terms of its uniformity, contrast, spatial resolution, noise power spectrum, and CT number linearity. Sample images of a skull phantom and a ham were also acquired using the DCBCT system to qualitatively illustrate high- and low-contrast resolution.

1.1.3 Four-dimensional CBCT

A tumor inside the body, especially in the lung and liver, can move during treatment. The recent development of four-dimensional (4D) CT [15] has made it possible to obtain volumetric information for tumors subject to respiratory motion. 4D CT provides respiratory correlated images, which represent different phases of the respiratory cycle. Sonke et al.[16] and Dietrich et al.[17] provided the proof-of-concept study of 4D CBCT in the 2005-2006. The projection data were acquired using conventional imaging protocols and the 4D images were reconstructed after sorting the projections for each respiratory phase. The scan time was 4 and 5.5 minutes, for the Sonke et al. and Dietrich et al. study, respectively. Recent 4D CBCT studies[7, 17-19] suffer from either poorly sampled phase images or very long scan time.

With the possible dual cone-beam CT, it is possible to reduce the scan time to achieve consistent, high quality 4D images. The focus of the work aims to develop a 4D-DCBCT technique to improve the efficiency of 4D imaging for motion management in radiation therapy.

1.1.4 Dual-Energy Imaging

The earliest investigation of dual-energy imaging for CT can be dated back to Alvarez et al.[20]. They presented that even by using a conventional polychromatic X-ray source, it is still possible to separate the attenuation coefficient into a photoelectric effect and Compton scattering component. In the diagnostic energy range, the X-ray attenuation is limited to the photoelectric effect and Compton scattering. Thus, the mass attenuation coefficient can be expressed as the linear combination of these two effects. It can also be expressed by the linear combination of the attenuation coefficients of two basis materials[21]:

$$ln(I/I_0) = -\mu_A(E)x_A - \mu_B(E)x_B \tag{1.1}$$

where $x_{A,B}$ and $\mu_{A,B}(E)$ represent the equivalent composition material thickness, in the unit of mm, and the linear attenuation coefficients, in the unit of mm^{-1}, of the object along the ray for material A and B, respectively.

For polychromatic beams with spectrum $S(E)$, the detected signal intensity can be expressed as:

$$ln(I/I_0) = \int S(E)[-x_A\mu_A(E) - x_B\mu_B(E)]dE \tag{1.2}$$

Dual-energy imaging usually requires two sets of projections of the same object using low- and high-energy beams. Pre- or post-reconstruction processing is then used to extract the spectral information for different applications depending on the imaging task. At present, dual-energy techniques have been developed and implemented primarily for conventional CT[12, 13, 21-25]. Limited work applying dual-energy techniques to CBCT has included micro-CT[26, 27] and research utilizing software-simulation platforms[28].

In comparison with conventional CT, CBCT suffers from increased X-ray scatter, reduced dynamic range and inferior detector quantum efficiency (DQE)[29-31]. Additionally, the polychromatic nature of the X-ray beam results in artifacts such as beam hardening and metal streaking in both conventional CT and CBCT. While previous research on dual-energy CT mainly focused on the development of new technology[32] or the implementation and evaluation of the technology[12, 13], this study focused on the latter to implement and evaluate the feasibility of dual-energy CT techniques for CBCT in the field of radiation oncology.

1.1.5 Kilovoltage/Megavoltage Imaging

Modern linear accelerators are typically equipped with both kV and megavoltage (MV) imaging devices readily mounted on the gantry. KV radiography and kV CBCT have already been proven to be powerful tools for improving localization accuracy in the treatment room for image-guided radiation therapy[18, 33]. Further, MV radiography and MV CBCT has the potential to provide complimentary advantages compared to kV imaging[34-36]. First, MV beams are attenuated less and therefore more suitable for penetrating through larger objects. Second, MV CBCT is less subject to metal artifacts caused by dental implants or hip prostheses. Therefore, an aggregated CBCT system that combines both kV and MV projections may provide better image quality over a system using only kV or only MV projections. Moreover, the data acquisition efficiency could be improved by acquiring kV and MV projections using an aggregated kV/MV scheme. Modern linear accelerators are typically equipped with both kV and MV imaging devices readily mounted on the gantry. By using an aggregated kV/MV acquisition scheme, the gantry only needs to rotate 110° to acquire sufficient data for CBCT reconstruction, thus reducing the rotation time roughly by a factor of 2. We investigated the possibility of dual cone-beam CT imaging using a kV and MV source, with the clinical LINAC illustrated in Figure 1-1(b). Specifically, the traditional dual-energy imaging technique used in diagnostic imaging was extended to reconstruct dual energy images with kV and MV energy sources.

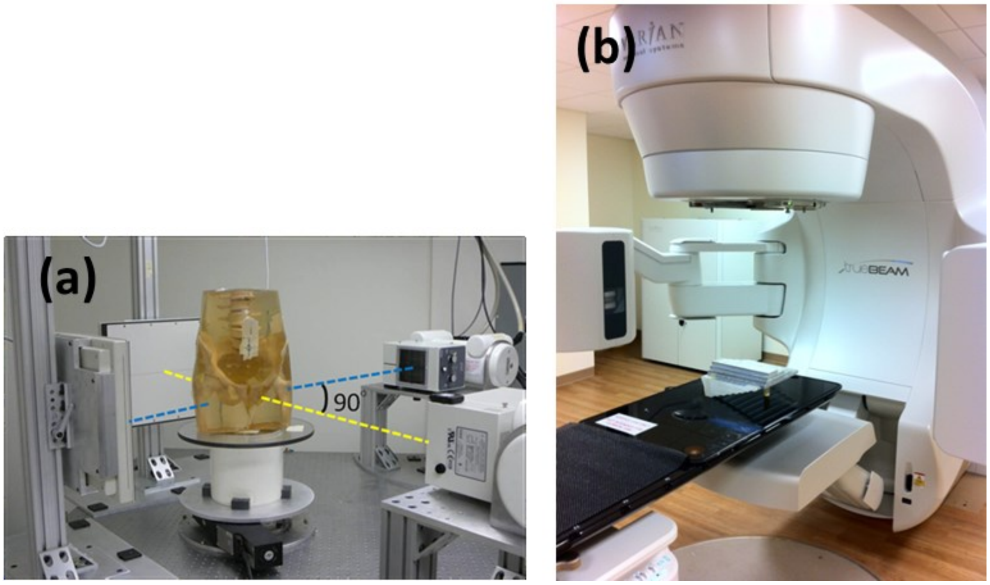

Figure 1-1 Systems using dual cone-beam CT geometry: (a) two sets of kV X-ray tube/detector, (b) LINAC with EPID with on-board imager

1.2 Overview of Chapters

Chapter 2: Initial Performance Characterization of a Dual Cone-Beam CT System provides the characterization of the DCBCT system. The findings presented in this chapter have been published in Medical Physics 40(2), Feb 2013.

Chapter 3: Four-Dimensional Dual Cone-Beam CT (4D-DCBCT): Preliminary Experimental Results investigated the four-dimensional imaging capabilities of dual-kV cone-beam CT. The findings presented in this chapter have been submitted for publication in Medical Physics, a peer-reviewed journal, and are currently under review.

Chapter 4: Implementation of Dual-Energy Technique for Virtual Monochromatic and Linearly Mixed CBCTs implemented the dual-energy imaging technique for CBCT imaging. The findings presented in this chapter have been published in Medical Physics 39(10), Oct 2012.

Chapter 5: Development of an Aggregated kV/MV Imaging Technique developed a novel imaging technique for kV/MV imaging. The findings presented in this chapter have been orally presented at 2012 ASTRO 54th Annual Meeting and submitted for publication in Medical Physics, a peer-reviewed journal, and are currently under review.

Chapter 6: Concluding Remarks provides a summary of the dissertation work.

2. Initial Performance Characterization of a Dual Cone-Beam CT System

2.1 Motivation

As mentioned in Section 1.1, CBCT using a kV source has been widely adopted for image-guidance in the treatment room to improve the accuracy of target localization, as it can be integrated on a LINAC. While kV CBCT provides high spatial resolution, improved soft tissue contrast as compared with kV radiography, and volumetric acquisition[2, 6-9], it still experiences a number of challenges. One complete CBCT acquisition using the on-board imager still takes approximately one minute, which renders a breath-hold CT scan difficult to implement[10].

In this study, a bench-top DCBCT system with two orthogonally placed tube/detector sets was developed. The DCBCT system may reduce the total scan time required, when compared to current single CBCT systems. Further, a dual cone-beam system could be configured with two non-coplanar imaging chains which may help alleviate cone-beam artifacts[37]. The DCBCT system would have potential to provide dual-energy imaging without the use of fast kV switching, which has already been recognized in dual-source diagnostic CT for its material differentiation and artifact reduction capabilities[11-13]. A dual cone-beam on-board imaging device would also allow for simultaneous, orthogonal radiographs[14], which have been shown to be highly useful in similar systems for target localization.

Single CBCT systems are routinely used for on-boarding imaging in radiation therapy treatment rooms and its imaging performance has been well evaluated[38]. However, very little information is available describing the imaging performance of a DCBCT system. A DCBCT system has additional sources for potential errors which do not exist in a single CBCT system that can degrade image quality, such as subsystem misalignments and differences in detector response.

One major concern for the DCBCT system is the cross scatter radiation between two CBCTs. The cross scatter is defined as the scatter cause by one X-ray source reaching the non-corresponding flat-panel detector. In simultaneous acquisition mode, the primary beam, the scattered photons, and the cross scatter radiation caused by the other source will reach the detector. A comprehensive characterization of the cross-scatter in DCBCT system can be found in a separate paper[39] and a measurement-based cross-scatter correction scheme has been proposed to suppress the effect of cross scatter[40].

In this chapter, we described the basic system configuration, imaging geometry, geometric calibration, and system performance of a prototype DCBCT system developed in our laboratory. The system performance was characterized in terms of its uniformity, contrast, spatial resolution, noise power spectrum, and CT number linearity. Sample images of a skull phantom and a ham were acquired using the DCBCT system to qualitatively illustrate high- and low-contrast resolution.

2.2 Methods

2.2.1 Prototype Bench-top System

2.2.1.1 System Configuration

The prototype DCBCT system (as shown in Figure 2-1(a)) consisted of two X-ray tubes (Varian G-242, Varian Medical Systems, Palo Alto, CA) and two large flat-panel detectors (PaxScan® 4030CB, Varian Medical Systems, Palo Alto, CA) together with a rotational stage in the middle for imaging objects. These components were mounted on an optical bench with an angular separation of 90° between two single CBCT systems. The X-rays tubes were powered by two CPI Indico 100 RF 50kW generators (Communications & Power Industries, Palo Alto, CA) and had an equivalent 0.7 mm aluminum filtration at the exit window. The collimator box for each X-ray tube consisted of two sets of adjustable blades along the horizontal and vertical directions and had an equivalent 2 mm aluminum filtration as specified by the manufacturer. Each flat-panel detector had a pixel area of 397x298 mm^2 and a pixel pitch of 194 μm. The detector allows different pixel binning modes and a maximal readout frame rate of 30 frames per second. The anti-scatter grid provided by the manufacturer was also mounted on the system to minimize scattered photons from the corresponding and orthogonal X-ray sources.

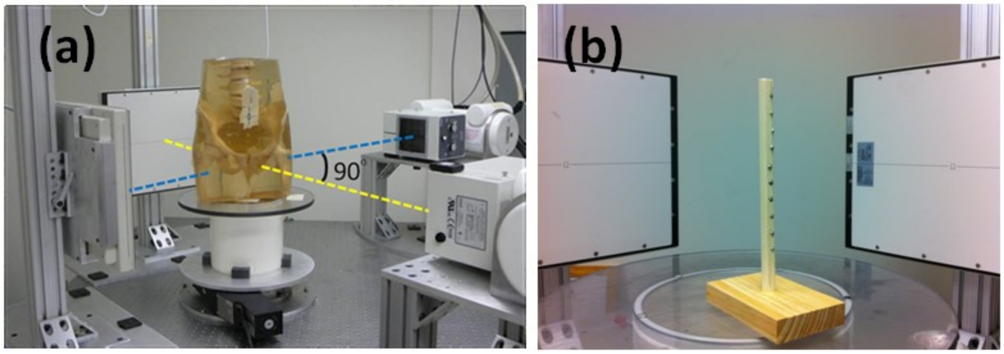

Figure 2-1 Photograph of the prototype DCBCT system (a) and the calibration phantom (b).

The X-ray tubes and detectors were located 100 cm and 50 cm away from the shared central axis, respectively, to mimic the typical imaging geometry of a single CBCT system mounted on the LINAC[41]. Since the imaging system is installed on an optical bench, long-term stability of the set-up is not an issue for this experiment. The flat-panel detectors were fixed such that the projection of the axis of rotation (AOR) lies in the center of the array. The cone angle for each imaging chain is about 9.5°. A summary of the system characteristics can be found in Table 2-1.

Table 2-1 Summary of characteristics of the prototype DCBCT system

DCBCT Characteristics	Values
Acquisition Geometry	
Subsystem 1:	
Source-axis distance	99.9cm
Source-imager distance	150.0cm
Subsystem 2:	
Source-axis distance	100.0 cm
Source-imager distance	150.2cm
Cone Angle	~ 9.5°
Field of View	26.7 cm

Angular Separation (measured)	90.6°
X-ray Beam	
Beam Energy (Maximal)	150 kV
Total Filtration	2.7 mm Al
Flat Panel Detectors	
Manufacture and Model	Varian Paxscan® 4030CB
Pixel Matrix	2048 x 1536
Pixel Pitch	194 μm
Effective Area	397 mm x 298mm
Fill Factor	70%
Limit Resolution	2.58 lp/mm @ 7.5 FPS (1x1) 1.29 lp/mm @ 30 FPS (2x2)
Conversion Screen	Integral columnar CsI:Tl
Receptor Type	Amorphous Silicon
Energy Range	40-150kVp
Reconstruction Parameters	
Reconstruction matrix	512x512x160
Voxel Dimension	0.488 mm x 0.488 mm x1 mm

2.2.1.2 Geometric calibration

In the past, for a single CBCT system, accurate geometric measurement was necessary to warrant high-quality image reconstruction. For the DCBCT system, not only must the accurate geometric measurement be acquired, but a few more uncertainties must be investigated, such as the angular separation and shift along rotational axis direction. It therefore becomes more challenging to calibrate the DCBCT system.

The DCBCT geometry requires the mapping of data from two flat-panel detectors onto one coordinate system for reconstruction. The geometric measurement was achieved by scanning an in-house calibration phantom with an array of metallic beads, as shown in Figure 2-1(b). The source-axis distance, source-imager distance, and angular separation between the two CBCT subsystems were then calculated using the methods developed by Johnston et al. and Yang et al.[42, 43]. The measured geometric parameters are also listed in Table 2-1.

2.2.1.3 DCBCT Acquisition

The DCBCT acquisition was controlled by the host computer which triggered both generators simultaneously. The objects were scanned through 200° of stage rotation, where the DCBCTs utilized 110° of projection data from one detector and 90° from the other and the single CBCTs utilized 200° data from each detector, as illustrated in Figure 2-2. The rotational stage kept spinning throughout the acquisition. Since there was no overlap between the two projection datasets, we did not employ any smooth transition between the two projection sets using weighting. Gain and offset corrections were implemented prior to scanning according to the manufacture recommendations.

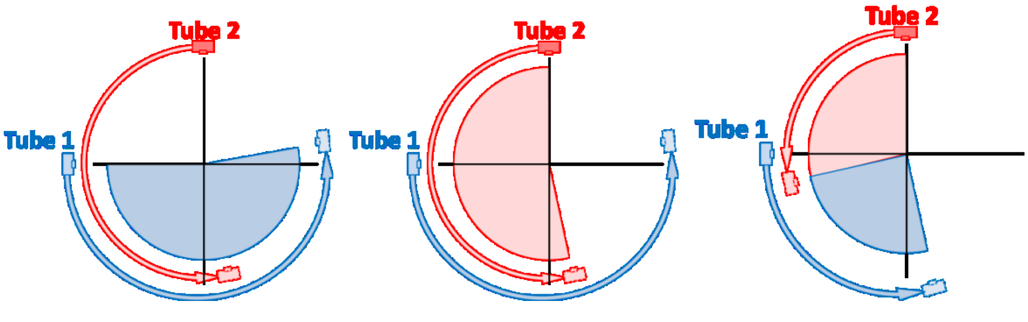

(a) (b) (c)

Figure 2-2 (a) Single CBCT acquisition from Tube 1 covering 200°, (b) Single CBCT acquisition from Tube 2 covering 200°, and (c) DCBCT acquisition from both Tubes (Tube 2: 110° and Tube 1: 90°).

The projection data acquired using the On-Board Imager (Varian Medical Systems, Palo Alto, CA) are initially read out from the flat panel detector after a 2x2 hardware binning and are then applied 2x2 software binning before CBCT reconstruction. Thus, for the convenience of comparison between the DCBCTs and clinical CBCTs in the future, the signal readout from the detector in our system was configured under the 2x2 binning mode and then additional 2x2 software binning, resulting in a 512x384 frame for each projection. No additional exposure was delivered before each frame to suppress the lag effect. The projection data from both detectors were normalized using the blank projection with corresponding in-house bow-tie filters.

The preprocessed projection data were used to reconstruct the CBCT using the FDK algorithm[44] filtered by a standard Hamming window with an α of 0.54. Projection data from both detectors were back-projected into one shared Cartesian coordinate. The reconstructed field of view (FOV) was 250x250x160 mm^3 for a matrix of 512x512x160. Similar to imaging parameters used for clinical CBCT reconstruction, the reconstruction voxel size was set to 0.488x0.488x1 mm^3. Upon completion of the reconstruction, a look-up table generated from the calibration phantom scanned under the same imaging parameters was applied to scale the voxel value to CT number.

2.2.1.4 Imaging Phantoms

A water phantom approximately 25 cm high and 20 cm in diameter was scanned to evaluate the uniformity and noise power performance, as shown in Figure 2-3(a). The contrast for different density objects and the CT number linearity were measured using the sensitometric slice of the CatPhan 504 phantom, as shown in Figure 2-3(b). The spatial resolution was measured using an in-house tungsten wire phantom of 0.125 mm diameter suspended vertically in a water bath, as shown in Figure 2-3(c). A skull phantom and a ham were scanned to evaluate high- and low-contrast response for qualitative evaluation of the overall performance of the system, as shown in Figure 2-3(d) and (e), respectively.

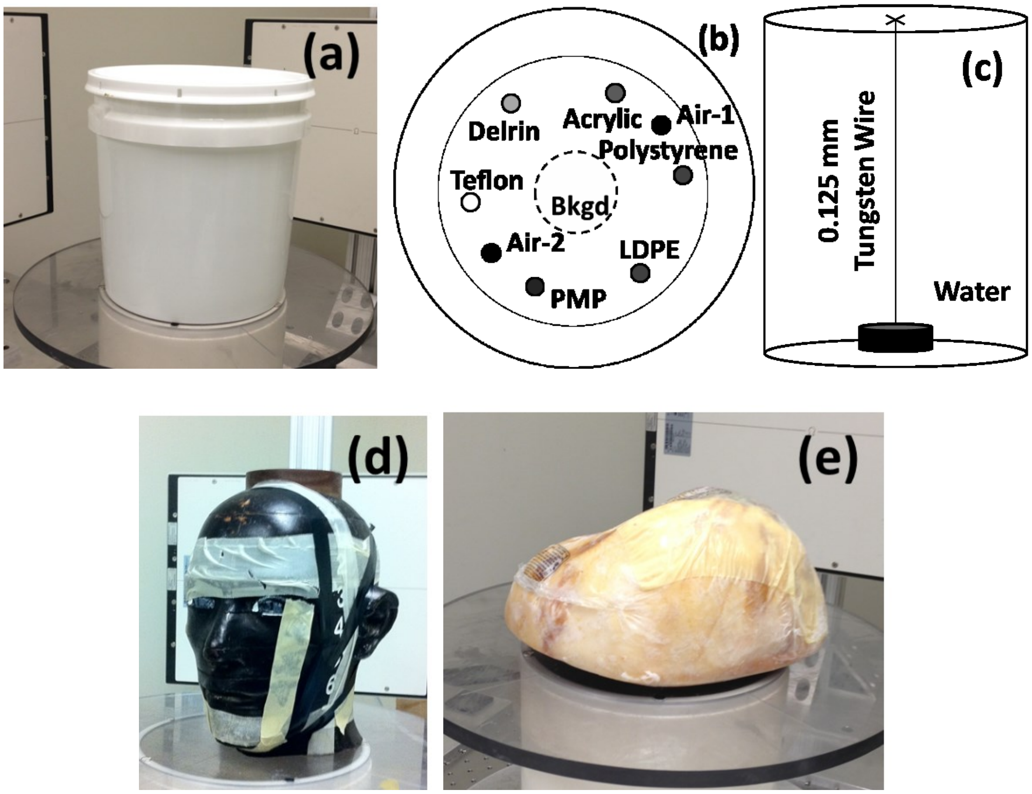

Figure 2-3 Phantoms used in the study: (a) water phantom, (b) sensitometric inserts in the Capthan, (c) tungsten wire phantom, (d) skull phantom, and (e) ham.

2.2.2 Performance Measurement

Since the major focus of this chapter is to address the imaging performance of the dual-source and single-source CBCT relative to each, we did not apply any additional scatter correction method except the anti-scatter grid originally installed on the flat panel detector, nor any beam-hardening correction.

2.2.2.1 Uniformity

The uniformity measurement was conducted using the following imaging parameters: a tube current 80mA and an exposure time of 20ms with four different energies: 80kV, 100kV, 125 kV and 150 kV. The response was examined in the central axial slice and also along the longitudinal direction. The uniformities for the axial slice and along the longitudinal direction were defined as:

$$Uniformity(Axial) = 100\% - \frac{|CTNum_1 - CTNum_2|}{|CTNum_1 - CTNum_{air}|} \tag{2.1}$$

$$Uniformity(Longitudinal) = 100\% - \frac{|CTNum_3 - CTNum_4|}{|CTNum_3 - CTNum_{air}|} \tag{2.2}$$

where $CTNum_{air}$ is the CT number for air, or -1000, and $CTNum_i$ (i = 1,2,3,4) are the CT number in region-of-interest (ROI) i in Figure 2-4.

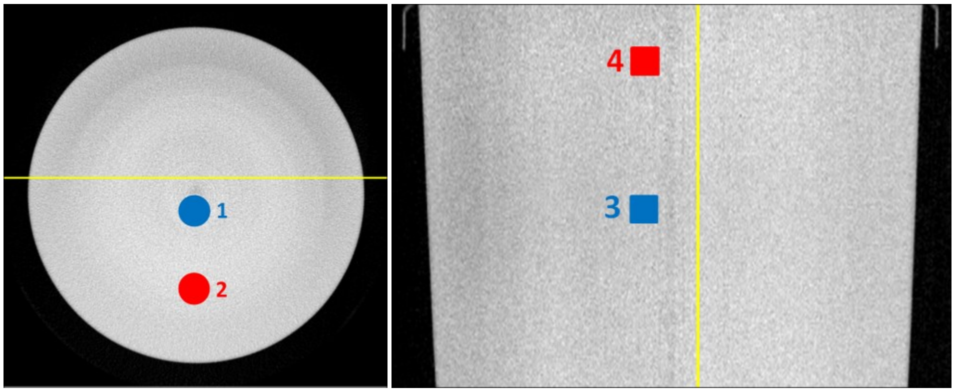

(a) **(b)**

Figure 2-4 Uniformity measurement for the water phantom: (a) Axial view, (b) longitudinal view.

2.2.2.2 Contrast-to-Noise Ratio

The contrast-to-noise ratio (CNR) was studied for different X-ray energies using the CatPhan 504 phantom. CBCT images were acquired using 80 mA and 20 ms for four different kV settings: 80kV, 100kV, 125kV and 150kV. The CNR values for 6 ROIs defined within the sensitometric inserts (excluding acrylic, which is the same material as the background), as shown in Figure 2-3(b), are then calculated as:

$$CNR = \frac{\left| avg.\ CT\ Number_{ROI} - avg.\ CT\ Number_{background} \right|}{Std.\ of\ CT\ Number_{background}} \qquad (2.3)$$

where the background is the central region in the axial slice. The background (acrylic) CT number is assumed to be 120 hounsfield unit (HU) and the CT number within the air ROI is assumed to be -1000 HU (ROI Air-1).

2.2.2.3 Spatial Resolution

The spatial resolution of the DCBCT system was evaluated using a tungsten wire test object with a diameter of 0.125 mm suspended in a cylindrical water bath, as shown in Figure 2-3(c). The wire was placed ~4 mm off-axis during acquisition to limit the influence of the ring artifact on the measurement. The CBCT image was reconstructed on a high-resolution grid of 0.1x0.1x0.1 mm^3 using the same filter as for a normal reconstruction. The point spread function was generated by averaging 6 adjacent slices to achieve a low noise background. The modulation transfer function (MTF) was then calculated based on the Gaussian-fitted point-spread-function (PSF) to limit the impact of noise on the results.

2.2.2.4 Noise Power Spectrum

The water bucket shown in Figure 2-3(a) was also scanned to assess the noise performance of the system using different energies. The structural fluctuations were removed by subtracting two identical scans taken sequentially. The three-dimensional noise power spectrum (NPS) was calculated using the 3D Fourier transform of a region of interest (ROI) of 10x10x10 cm^3 using the following equation[45]:

$$NPS(u,v,w) = \frac{1}{N}\sum_{i=1}^{N}\frac{[DFT_{3D}(DI_i(x,y,z)-\overline{DI_i})]^2}{2}\frac{\Delta x}{N_x}\frac{\Delta y}{N_y}\frac{\Delta z}{N_z} \qquad (2.4)$$

where N is the number of ROIs within the measurement volume, $DI_i(x,y,z)$ is the value of voxel (x,y,z), $\overline{DI_i}$ is the mean value of $DI_i(x,y,z)$, N_x, N_y, N_z are the number of voxels, and $\Delta x, \Delta y, \Delta z$ are voxel pitches along x, y, z directions, respectively.

The NPS of the subtracted image differed from the original image by a factor of 2[46] and is reflected in the calculation of NPS in Eq. (2.4). $DI_i(x, y, z)$ and $\overline{DI_i}$ in Eq. (2.4) are voxel values in the subtracted images. Two identical reconstructed axial slices and their subtracted image are shown in Figure 2-5. The radial average is then calculated at every degree in the central slice of the 3D Fourier space to reduce the measurement fluctuation. The profile of the radial average was used to compare dual and single detectors at different kVp (80, 100, 125, and 150 kVp) with the same mAs (80 mA and 20 ms).

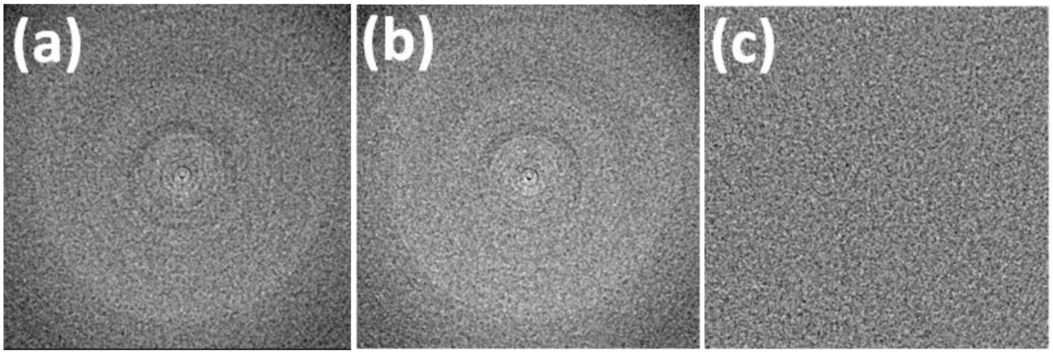

Figure 2-5 (a-b) reconstructed slices of two identical scans, (c) subtracted image of two scans.

2.2.2.5 CT Number Linearity

Seven high contrast sensitometric targets in the Catphan phantom, were used to evaluate the CT number linearity response of the system, as shown in Figure 2-3(b). These targets ranged from approximately -1000 HU to +1000 HU. Table 2-2 summarizes the material used in these targets and the corresponding CT number.

Table 2-2 Sensitometric Inserts in the CatPhan

Material	CT Number
Air	-1000
Polymethylpentene (PMP)	-200
Low density polyethylene (LDPE)	-100
Polystyrene (PS)	-35
Acrylic	120
Delrin	340
Teflon	990

2.2.2.6 Qualitative Phantom Study

To demonstrate the high-contrast and low-contrast resolution of the system, a skull phantom and a ham were scanned using the DCBCT system, as shown in Figure 2-3(d) and (e), respectively. The skull phantom and the ham have a diameter of approximately 15 cm and height of approximately 20cm.

2.3 Results

2.3.1 Imaging Performance

2.3.1.1 Geometric Calibration

The geometric calibration is critical for the system performance. To qualitatively demonstrate this, the reconstructed slices using the DCBCT system with and without geometric calibration of the Catphan phantom containing the bar patterns are demonstrated in Figure 2-6(b) and (c), respectively. The same phantom imaged by a single CBCT system is also shown in Figure 2-6(a) for comparison. The bar patterns as shown in Figure 2-6(a) and (b) are easily identifiable with proper geometric calibration. Ring artifacts were observed in Figure 2-6(b) due to the differences in sensitivity between the two flat-panel detectors. The image quality is severely compromised if no geometric calibration is performed as shown in Figure 2-6(c).

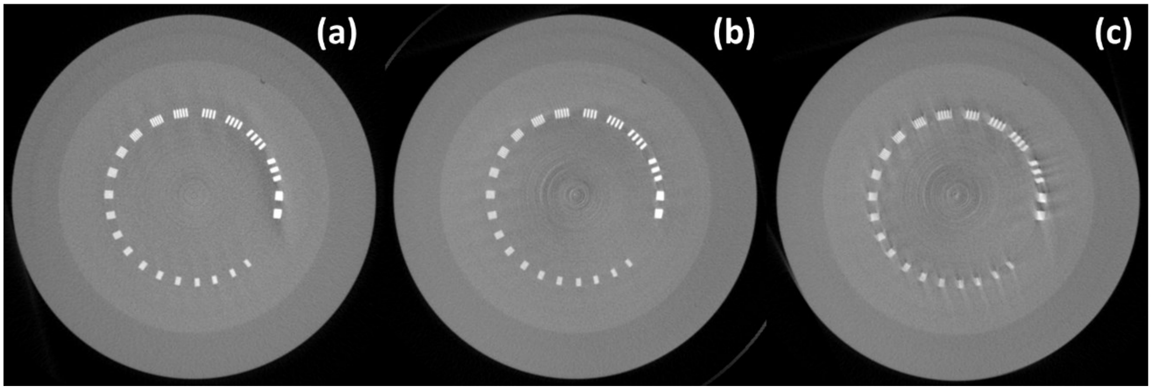

Figure 2-6 Bar patterns in the Catphan phantom: (a) single CBCT with geometric calibration, (b) DCBCT with geometric calibration, and (c) DCBCT without geometric calibration.

2.3.1.2 Uniformity

The uniformity in both the radial and longitudinal direction is shown in Figure 2-7 for the DCBCT compared with single CBCT. The line profiles of the Catphan at the central slice for different energies (80kV, 100kV, 125kV and 150kV) are plotted in Figure 2-7(a)-(d), respectively. The line profiles along the longitudinal direction for four different energies are plotted in Figure 2-7(e)-(f).

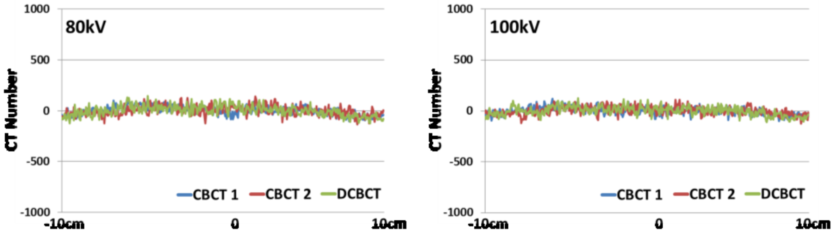

(a) (b)

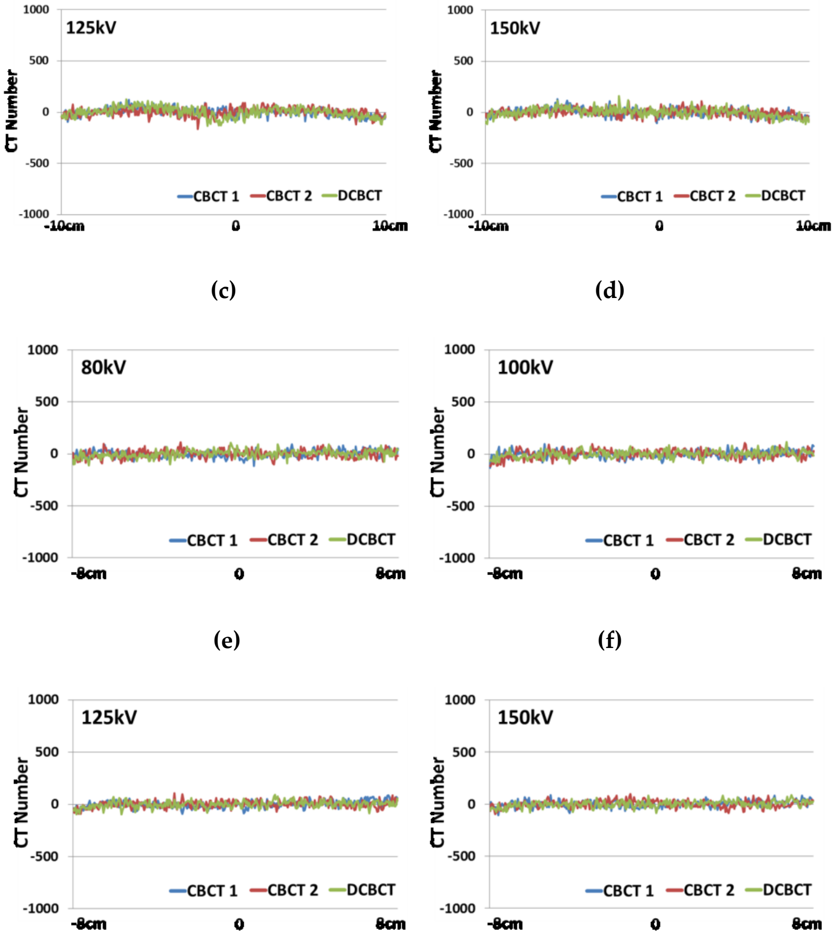

(c) (d)

(e) (f)

(g) (h)

Figure 2-7 Uniformity profile for the water phantom: (a)-(d) axial profile for 80kV, 100kV, 125kV and 150kV, (e)-(h) longitudinal profile for 80kV, 100kV, 125kV and 150kV.

Table 2-3 summarizes the uniformity measurements for both the axial and longitudinal directions for four different energies. An average of 1.9% axial and 1.1% longitudinal decrease in uniformity for DCBCT compared with single CBCT were measured. We believe the decrease of uniformity in the DCBCT is related to the non-homogeneity and cross-scatter between the two single CBCT systems. The two single

CBCT systems have different detector responses. Thus when mapping the projection data from two single CBCTs into one coordinate system, this difference could degrade the uniformity in the DCBCT. The effect of cross-scatter between the two single CBCTs systems has been studied in details by Giles et al [23].

Table 2-3 Uniformity for Dual and Single CBCT along Axial and Longitudinal View

	Axial			Longitudinal		
	DCBCT	CBCT 1	CBCT 2	DCBCT	CBCT 1	CBCT 2
80 kV	95.7%	98.7%	98.3%	98.3%	99.3%	98.1%
100 kV	96.9%	99.1%	99.3%	97.6%	99.6%	99.7%
125 kV	97.5%	99.4%	97.6%	98.1%	99.7%	98.2%
150 kV	98.2%	99.7%	99.6%	98.2%	99.3%	99.1%

2.3.1.3 Contrast-to-Noise Ratio (CNR)

The CNR values for different photon energies are demonstrated in Figure 2-8. The CNR values calculated within selected ROIs shown in Figure 2-8(a) are presented according to the different acquisition kV values. Figure 2-8(b) to (e) shows CNR values calculated from the CBCT images acquired using two single detectors and both detectors with nominal kV energies of 80kV, 100kV, 125kV and 150kV, respectively. For low-contrast inserts, e.g. polystyrene and LDPE, comparable CNR for DCBCT was observed for four tested energies in comparison with single CBCT within the range of measurement fluctuation.

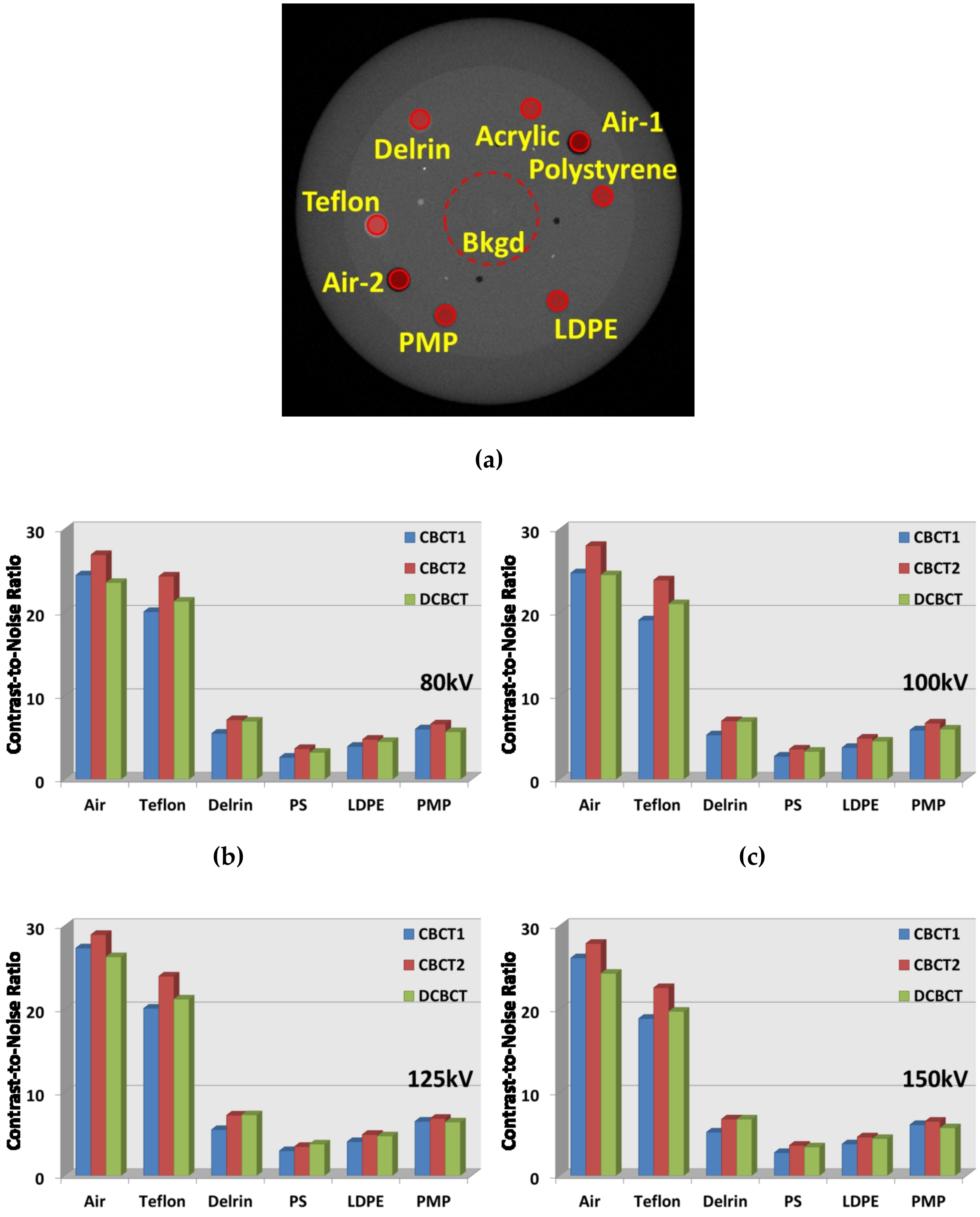

(a)

(b)

(c)

(d)

(e)

Figure 2-8 Contrast-to-noise ratio: (a) Reconstructed axial slice of sensitometric inserts, (b)-(e) CNR measurements for 80kV, 100kV, 125kV and 150kV.

2.3.1.4 Spatial Resolution

The system response of the tungsten wire is illustrated in Figure 2-9. Figure 2-9(a) presents the reconstructed results of the tungsten wire with a selected ROI of 4x4 mm^2 square surrounding the tungsten wire for the DCBCT and single CBCT, respectively. The MTF profiles for the dual and single CBCTs are overlapped and shown in Figure 2-9(b). In our study, the MTFs at 10% is around $1mm^{-1}$ for both the dual and single CBCT systems. This comparison suggests that a comparable spatial resolution can be achieved in the DCBCT system in comparison with the single CBCT system.

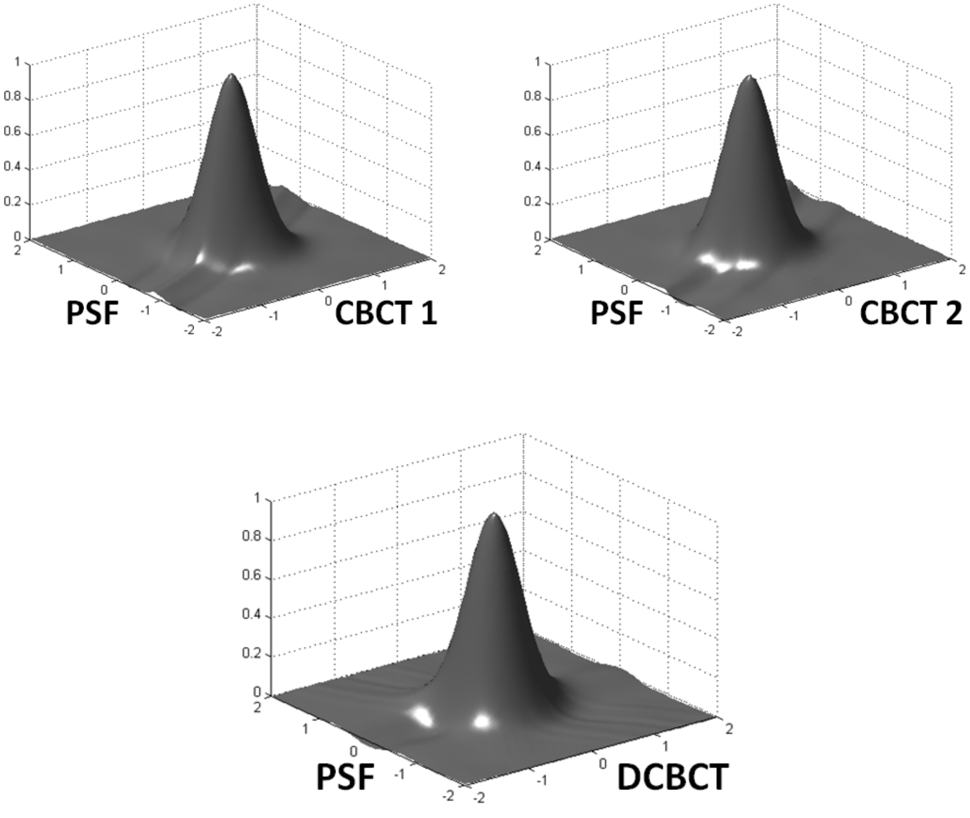

(a)

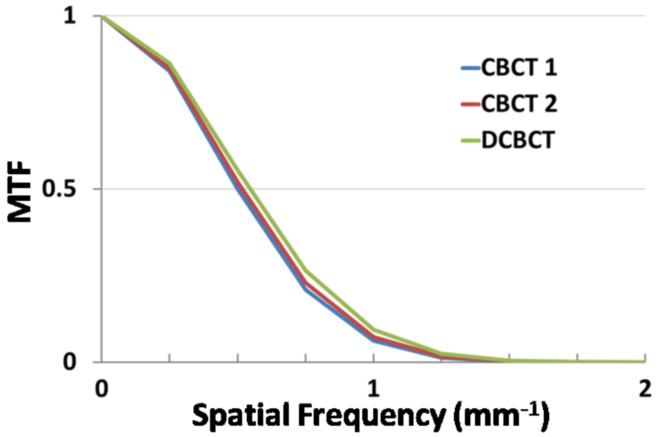

(b)

Figure 2-9 Spatial resolution for dual and single CBCT image of tungsten wire: (a) PSF, (b) MTF.

2.3.1.5 Noise Power Spectrum

The axial, coronal, and sagittal views of the 3D NPS are shown in Figure 2-10. These data demonstrate a radial symmetry of the NPS in the axial plane, which provides validation for radial averaging to convert 2D NPS into the 1D NPS in the study. The radially-averaged profiles for the DCBCT and single CBCT are plotted in Figure 2-11. It can be seen that the shape of both profiles are almost identical. The DCBCT, however, has a smaller value in magnitude compared with the single CBCT results.

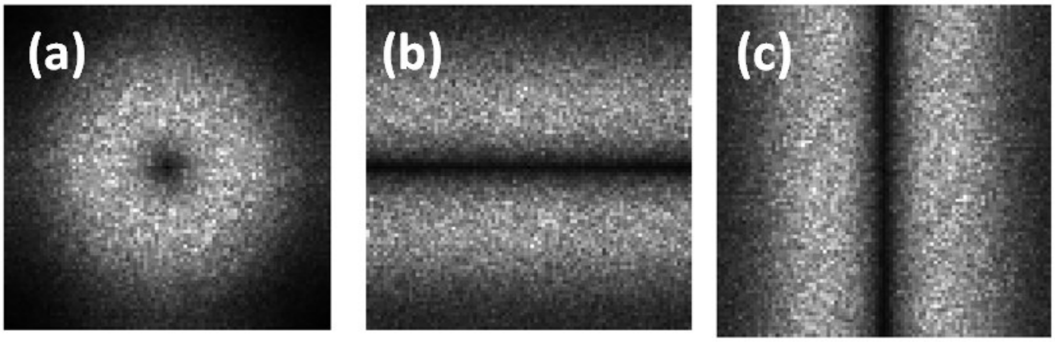

Figure 2-10 3D NPS result: (a) axial slice, (b) sagittal slice, and (c) coronal slice.

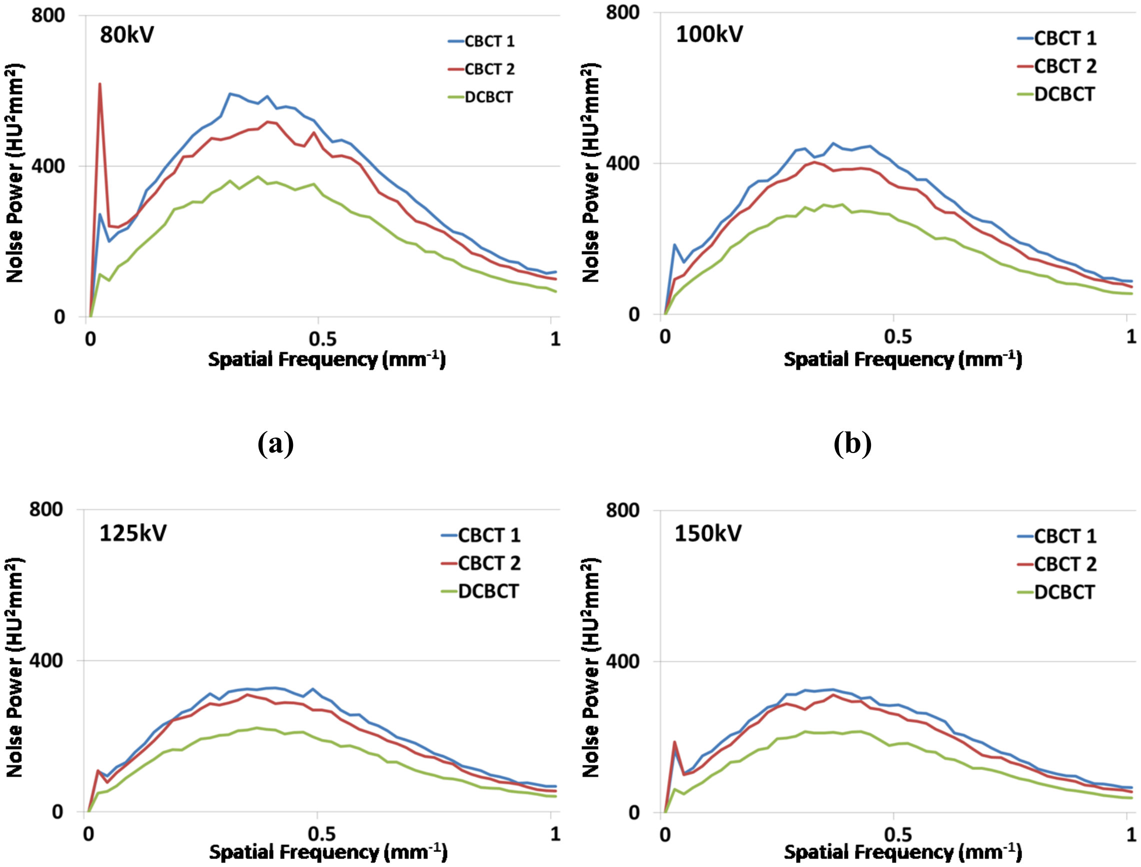

(a)

(b)

(c)

(d)

Figure 2-11 Radially-averaged NPS measurement with the same mAs (80mA, 20ms) at different energies: (a) 80kV, (b) 100 kV, (c) 125 kV, and (d) 150 kV.

2.3.1.6 CT Number Linearity

The reconstructed axial slice of the seven high contrast sensitometric targets in the Catphan phantom are shown in Figure 2-8(a). The mean voxel value of each target is measured in a circular ROI with the diameter of 3mm. To analyze the system comprehensively, we also discussed the linear response under different energies (80kV, 100kV, 125kV and 150kV) in Figure 2-12(a)-(d). A strong linear correlation exists between the mean voxel values of the ROIs and known contrast target's concentration for DCBCT, even though the linear regression slope is different from the single CBCT's. The coefficient of determination R^2 was calculated for each linear fitting and the results are summarized in Table 2-4. It can be easily observed that DCBCT system has shown comparable strong linear response with R^2 greater than 0.99 for all four energies despite different regression slope.

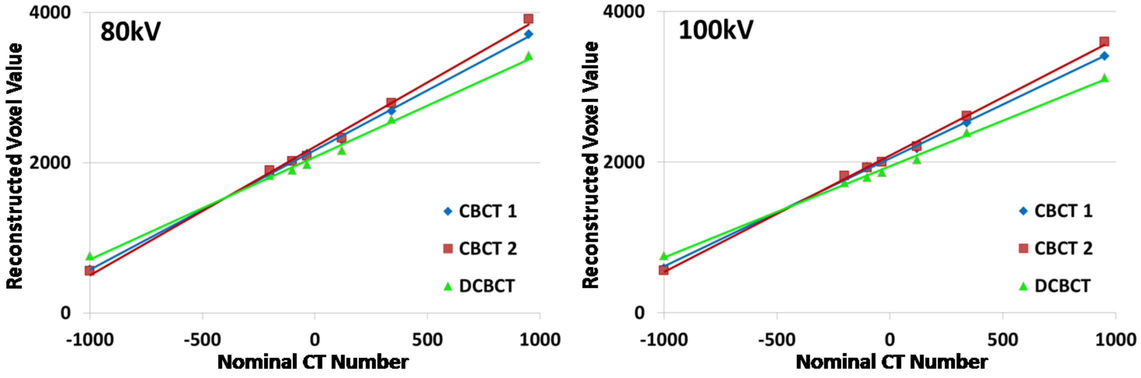

(a) **(b)**

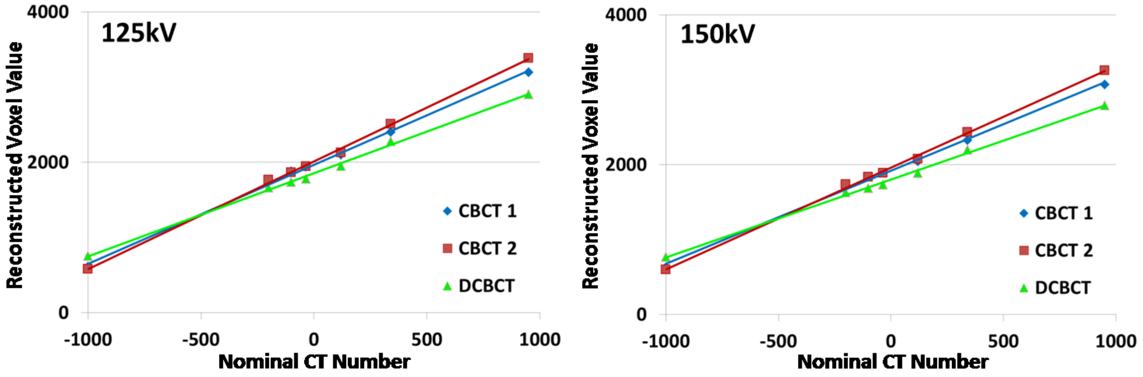

(c) (d)

Figure 2-12 Linearity measurement: (a)-(d) linear regression fits for single subsystem under 80kV, 100kV, 125kV and 150kV, respectively.

Table 2-4 R^2 of CT Number Linearity.

	DCBCT	CBCT 1	CBCT 2
80 kV	0.9956	0.9964	0.9989
100 kV	0.9974	0.9982	0.9988
125 kV	0.9977	0.9987	0.9982
150 kV	0.9975	0.9986	0.9976

2.3.2 Phantom Scan Illustration

Finally, the in-vitro scan of the skull phantom and ham were acquired to visually demonstrate the overall performance of the DCBCT system, as shown in Figure 2-13 and Figure 2-14. The images of the skull phantom in Figure 2-13 clearly demonstrate the high spatial resolution of the system. Example images are shown for the central axial, coronal and sagittal views generated with the DCBCT system. Fine details of the bony structures of the skull are easily identifiable. A ham was also scanned and a few example CBCT axial views are shown in Figure 2-14, which demonstrate the clear visualization of soft tissue (e.g. muscle, fat) with high spatial resolution.

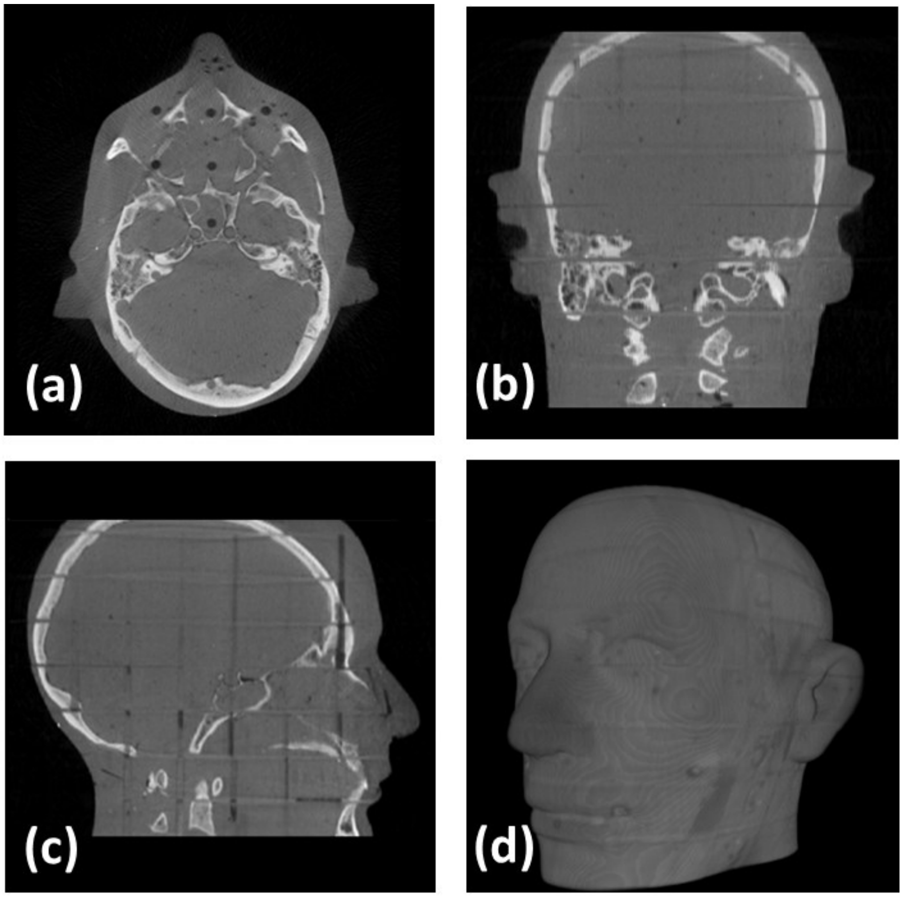

Figure 2-13 DCBCT images of the skull phantom: (a) axial view, (b) coronal view, (c) sagittal view, and (d) 3D surface rendering.

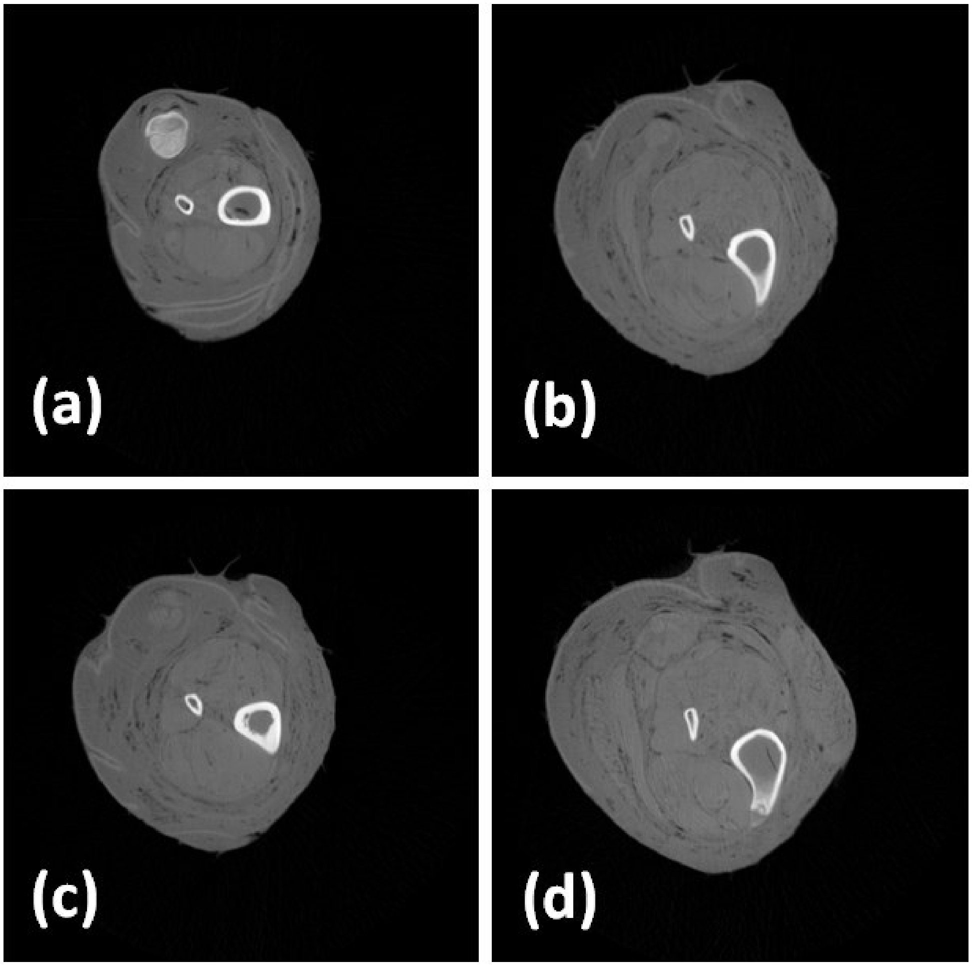

Figure 2-14 (a)-(d) Example axial slices of DCBCT images for the ham.

2.4 Discussion

This chapter mainly investigates the feasibility of constructing an orthogonally arranged DCBCT system and its system performance. The quantitative and qualitative results of our studies suggest that the DCBCT system is a promising candidate for high performance computed tomography with faster acquisition time with comparable performance to the single CBCT system. Two X-ray sources are placed in orthogonal directions to mimic the geometry of the on-board kV imager and MV beam imager. In this set-up, the object needs to rotate 110° to provide a 200° coverage for reconstruction, as shown in Figure 2-2. The CBCT reconstruction using a dual source is also readily available using kV and MV beams with no additional hardware requirement[47-50]. No significant degradation in the performances of uniformity spatial resolution and CT number linearity for the DCBCT system were observed when comparing to a single CBCT system. Good linearity has been demonstrated between the reconstructed pixel values of the contrast targets and known CT numbers. Further, the results from the phantom scans show high spatial resolution and good soft tissue contrast.

The DCBCT system opens up many potential applications for IGRT, e.g. faster imaging and dual-energy CT imaging. With two orthogonal X-ray beams imaging the same patient volume, a quarter scan is sufficient to reconstruct the images. The scan time can be reduced by approximately half, and it becomes feasible for some patients to hold their breath during the thoracic and abdominal scans. This can significantly reduce motion artifacts.

The two X-ray tubes can be operated at different voltages and therefore provide dual energy capability. Moreover, under new acquisition strategies, the DCBCT system can be flexibly applied to multi-energy imaging, such as continuous kV switching, to obtain associated benefits with multi-tiered contrast resolution and material differentiation.

The imaging dose from the DCBCT may not be necessarily higher than that from the single CBCT system. Using the acquisition scheme proposed in Figure 2-2, the DCBCT system acquires the same total number of projections when compared with a single CBCT system covering 200°. Assuming that each projection is acquired with a fixed mAs/kVp and no angular overlap during acquisition, the imaging dose from the DCBCT acquisition should be identical to that from the single CBCT system.

2.5 Conclusion

This study described a prototype DCBCT imaging system and characterized the imaging performance of a successful implementation of the DCBCT system using large flat panel detectors.

3. Four-Dimensional Dual Cone-Beam CT (4D-DCBCT): Preliminary Experimental Results

3.1 Motivation

The accurate delivery of radiation to moving tumors, such as lung cancer, presents a challenge in the motion management in radiation therapy. Four-dimensional cone-beam CT (4D-CBCT) is one example that allows motion assessment by providing volumetric information during each respiratory cycle[7, 17, 51-53]. One of the major challenges for clinical implementation of 4D-CBCT is the long scan time. This chapter aims to develop a 4D-DCBCT technique to improve the efficiency of 4D imaging for motion management in radiation therapy.

3.2 Materials and Methods

3.2.1 Dual Cone-Beam CT System Description

The prototype DCBCT system is the same as described in Section 2.1.1 (as shown in Figure 3-1(a)). The objects were scanned through 200° of stage rotation, where the dual CBCTs utilized 110° of projection data from one detector and 90° from the other and the single CBCTs utilized 200° of data from each detector, as illustrated in Figure 3-1(b)-(d).

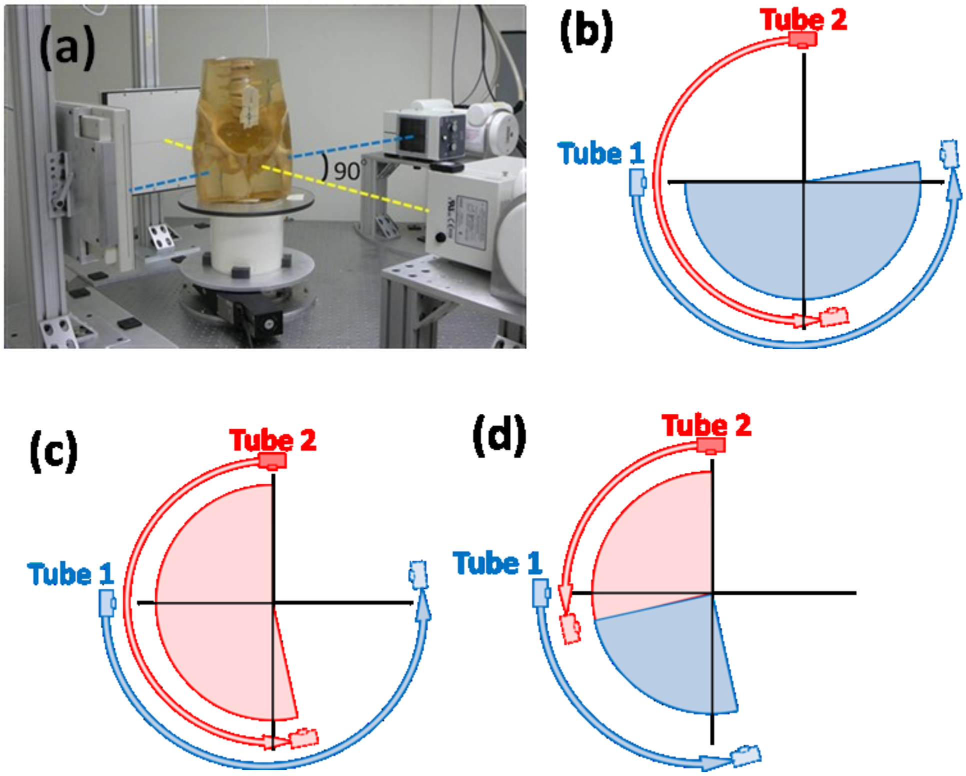

Figure 3-1 (a) Picture of the prototype DCBCT system, (b) Single CBCT acquisition from Tube 1 covering 200°, (c) Single CBCT acquisition from Tube 2 covering 200°, and (d) Dual CBCT acquisition from both Tubes (Tube 2: 110° and Tube 1: 90°).

3.2.2 Scan Time Reduction

The experiments were designed to test two hypotheses for the potential advantages of the 4D-DCBCT system: scan time reduction, and better temporal correlation/less respiratory variation.

For the scan time reduction, the 4D data acquisition time(AT) can be calculated using Eq. (3.1), where SA is the scan angle, RC is the respiratory cycle, PW is the phase window and AI is the angular interval[54]. The AT can be reduced by nearly a factor of two as a direct consequence of the reduction in SA from 200° to 110°.

$$AT = \frac{SA\times RC_{100}\times(1+\frac{PW}{100})}{AI_{100}} \tag{3.1}$$

To prove the effect of reduced scan time, a sphere embedded in a cylinder was imaged on a motion phantom platform driven by a simple sinusoidal wave with a period of 5 seconds, as shown in Figure 3-2(a). The normalized mutual information (NMI) was calculated between phase pairs of the 4D-DCBCT and two single 4D-CBCTs.

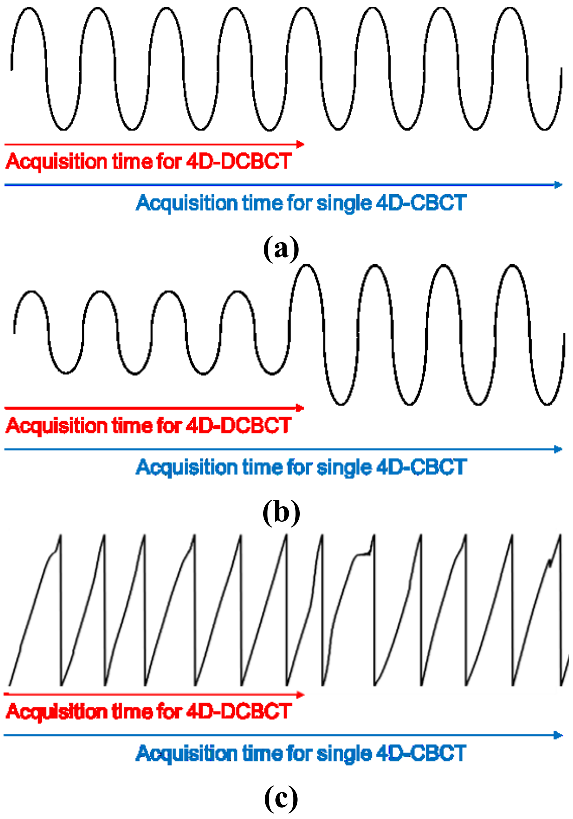

Figure 3-2 Profiles for motion phantom input: (a) simple sinusoidal wave, (b) irregular sinusoidal wave, and (c) illustrative patient respiratory profile.

3.2.3 Better Temporal Correlation/Less Respiratory Variation

The temporal correlation and respiratory variation was studied by scanning the same phantom with different profiles, as shown in Figure 3-2(b) and (c). Figure 3-2(b) is a sinusoidal profile with an increase in amplitude for the second half of the acquisition. Figure 3-2(c) is an illustrative profile derived from a patient case.

3.3 Results

3.3.1 Scan Time Reduction

Sagittal views of 10 different phase windows for two single 4D-CBCTs and the 4D-DCBCT are shown in Figure 3-3(a). The NMI values are summarized in Table 3-1. The average NMIs of 10 phase windows between 4D-DCBCT and two single 4D-CBCT (0.331, and 0.320) are very close to the NMI between two single 4D-CBCTs (0.336).

Table 3-1 NMIs for each phase window using a simple sinusoidal wave profile

NMI for each phase window	0%-10%	10%-20%	20%-30%	30%-40%	40%-50%	50%-60%	60%-70%	70%-80%	80%-90%	90%-100%	Average of 10 phase windows
4D-CBCT 1st vs. 2nd	0.358	0.368	0.343	0.304	0.297	0.330	0.363	0.366	0.333	0.301	0.336
4D-DCBCT vs. 1st 4D-CBCT	0.354	0.360	0.338	0.300	0.294	0.322	0.352	0.355	0.331	0.306	0.331
4D-DCBCT vs. 2nd 4D-CBCT	0.338	0.343	0.325	0.286	0.288	0.315	0.345	0.345	0.320	0.290	0.320

3.3.2 Better Temporal Correlation/Less Respiratory Variation

For the irregular sinusoidal case, it can be easily observed that 4D-DCBCT has shown much less motion blurring in different phase windows (Figure 3-3(b)), e.g. 0%-10%, 80%-90%. For the patient profile (Figure 3-3(c)), the breathing variation is not significant for the selected patient, thus less prominent comparison was observed using the patient profile.

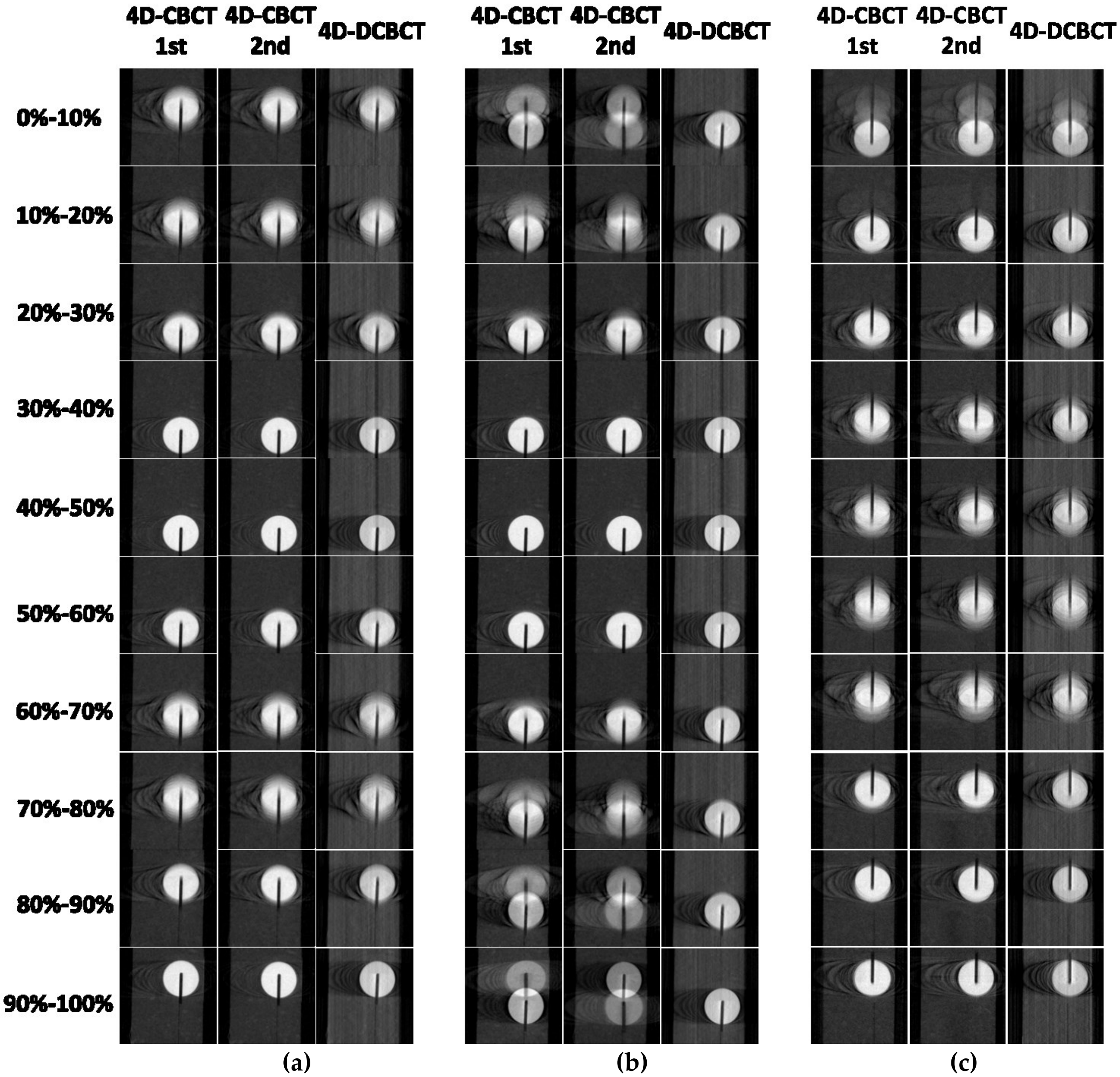

Figure 3-3. Sagittal view of different phase windows using (a) simple sinusoidal wave (Figure 3-2(a)), (b)irregular sinusoidal wave (Figure 3-2(b)), and (c) patient respiratory profile (Figure 3-2(c)).

3.4 Discussion

The temporal resolution is improved in two ways: 1) short acquisition time; and 2) simultaneous acquisition between two detectors. For the simple sinusoidal wave profile, 4D-DCBCT provided similar visual image and normalized mutual information for each respiratory phase compared with the regular 4D-CBCT. For the irregular sinusoidal wave in our study, the 4D-DCBCT generated a less blurry image because less motion was introduced during the reconstruction as the result of the reduced scan time.

Note that the CBCT acquired with reduced scan time and thus with less motion blur may potentially not reflect the real scenario during treatment, especially for irregular breathing patterns. The information with larger motion amplitude may not be included for the short scan time. A longer scan time leads to more image blurring for regular 4D-CBCT, but may avoid underestimation of the total motion range of the tumor, when compared to the proposed 4D-DCBCT. However, one can reduce the rotation speed to ensure a longer acquisition time. Therefore, 4D-DCBCT provides the flexibility to choose between short or long scan times. It is up to users' discretion to apply this technique in the clinical settings.

The results using the patient profile shown in Figure 3-3(c) did not show substantial differences between the single CBCTs and DCBCT. Even though the most irregular patient-derived breathing profile was used, the patient breathing still did not change as dramatically as the profile provided in Figure 3-3(b). This also means that for real patient cases, DCBCT can provide similar results when compared with the single CBCT, while at the same time reducing the scan time by half.

3.5 Conclusions

Comparable image quality in terms of mutual information can be achieved using 4D-DCBCT with a reduction in scan time by half when compared with 4D-CBCT. Due to the reduction in scan time, 4D-DCBCT can produce less blurry images of each respiratory phase for irregular breathing profiles.

4. Implementation of Dual-Energy Technique for Virtual Monochromatic and Linearly Mixed CBCTs

4.1 Motivation

In comparison with conventional CT, CBCT suffers from increased X-ray scatter, reduced dynamic range and inferior detector quantum efficiency (DQE)[29-31]. Additionally, the polychromatic nature of the X-ray beam results in artifacts such as beam hardening and metal streaking in both conventional CT and CBCT. Researchers have proposed many methods to reduce the effects of metal artifacts in conventional CTs[55-58] but only recently has metal artifact reduction in CBCT received attention in the literature[59, 60]. There are two approaches for metal artifact reduction in both CT and CBCT, the feature based and spectrum based approaches. The feature based technique includes pre-processing of the projection images by masking off metal features in each projection[55, 56, 58, 60]. This approach requires prior knowledge of the metal structure and the locations and is limited when this information is uncertain or unavailable. On the other hand, the spectrum based technique applies a dual energy technique to generate a virtual monochromatic energy CT to minimize the metal artifacts[61]. Reported metal artifact reduction techniques for CBCTs have so far only used the feature based techniques[60].

Dual-energy imaging usually acquires two sets of projections using low- and high-energy beams scanning the same object. Pre- or post-reconstruction processing is then used to extract the spectral information for different applications depending on the imaging task. Presently, dual-energy techniques have been developed and implemented primarily for conventional CT[12, 13, 21-25]. Limited work applying dual-energy techniques to CBCT has included micro-CT[26, 27] and research utilizing software-simulation platforms[28]. While previous research of dual-energy CT mainly focused on the development of new technology[32] or the implementation and evaluation of the technology[12, 13], this study focused on the latter to implement and evaluate the feasibility of dual-energy CT techniques for CBCT in the field of radiation oncology. Previously, the utility and advantages of dual-energy CBCT imaging with a large flat-panel detector configuration for radiation therapy had not been well understood. In this study, we utilized an in-house bench-top CBCT system consisting of a large flat-panel detector, similar to those employed for onboard imaging in radiation therapy, to implement dual-energy techniques relevant to radiation therapy. Specifically, we evaluated the two techniques that are commonly applied in dual-energy conventional CT imaging: virtual monochromatic (VM) and linearly mixed (LM) CBCTs.

In the VM technique, a single set of monochromatic CBCTs is synthesized using the dual-energy projection data, originally proposed by Alvarez et al[62]. The basic work flow involves basis material decomposition before reconstruction and linear combination of density maps for the decomposed images. In principle, artifacts caused by beam hardening and photon starvation can be removed. This artifact reduction is one of the major benefits of the VM application in diagnostic CT[63]. In this study, we evaluated the effectiveness of metal artifact reduction using the VM technique with an in-house titanium-BB phantom. For iodine contrast in metal-free objects, the optimal monochromatic energy selection to maximize the CNR in VM CBCTs was studied using a water phantom containing two iodine concentrations.

In the LM technique, a single set of CBCTs was generated from a linear combination of low- and high-energy CBCTs. Instead of using material-specific imaging or dual-energy radiography subtraction, the low- and high-energy CBCTs are added in the LM technique. The image quality of LM CBCTs from dual-energy scans was evaluated in terms of noise and contrast-to-noise ratio (CNR) and compared with single-energy CBCTs on an equal dose basis. The weighting factors for LM CBCTs were optimized to either minimize noise or maximize CNR at various radiation dose partitioning schemes and the results were compared with single-energy scans performed at 80, 100, 125 and 150kVp with equal dose.

4.2 Materials and Methods

4.2.1 Generation of Virtual Monochromatic CBCT

4.2.1.1 Basis Material Decomposition

4.2.1.1.1 Theory

In the diagnostic X-ray energy range, the attenuation coefficient of a material can be decomposed into a photoelectric and a Compton scatter component. Since these two components are difficult to measure independently, they are practically approximated with two basis materials, one with relatively high atomic number Z and the other with relatively low Z. For a given energy, the high Z and low Z material have different compositions of photoelectric effect and Compton scatter components, which can be differentiated using the dual-energy technique. The attenuation along a ray can be written as a linear combination of these two basis materials A and B for an incident radiation I_0 and an exit radiation I[62, 64]:

$$ln(I/I_0) = -\mu_A(E)x_A - \mu_B(E)x_B \tag{4.1}$$

where $x_{A,B}$ and $\mu_{A,B}(E)$ represent the equivalent composition material thickness, in the unit of mm, and the linear attenuation coefficients, in the unit of mm^{-1}, of the object along the ray for material A and B, respectively.

Two measurements I_L and I_H acquired with monochromatic beams at two different energies E_L and E_H can therefore be expressed as[62, 64],

$$\begin{cases} ln(I_L/I_0) = -x_A\mu_A(E_L) - x_B\mu_B(E_L) \\ ln(I_H/I_0) = -x_A\mu_A(E_H) - x_B\mu_B(E_H) \end{cases}. \tag{4.2}$$

From these two equations it follows that,

$$\begin{bmatrix} x_A \\ x_B \end{bmatrix} = \begin{bmatrix} -\mu_A(E_L) & -\mu_B(E_L) \\ -\mu_A(E_H) & -\mu_B(E_H) \end{bmatrix}^{-1} \begin{bmatrix} ln(I_L/I_0) \\ ln(I_H/I_0) \end{bmatrix} \tag{4.3}$$

However, for polychromatic beams with low-energy spectrum $S_L(E)$ and high energy spectrum $S_H(E)$, the measurements I_L and I_H can be written as[62, 64]:

$$\begin{cases} ln(I_L/I_0) = \int S_L(E)[-x_A\mu_A(E) - x_B\mu_B(E)]dE \\ ln(I_H/I_0) = \int S_H(E)[-x_A\mu_A(E) - x_B\mu_B(E)]dE \end{cases}. \tag{4.4}$$

Eqs. (4.4) are generalizations of Eqs. (4.2) since they include integrals over the beam energy spectrum. In practice, it is difficult to obtain analytical solutions for Eqs.

(4.4). Thus, an approximate solution proposed by Cardinal et al. in [65] was used in the study:

$$
\begin{aligned}
x_A &= \frac{a_0+a_1L+a_2H+a_3L^2+a_4LH+a_5H^2}{1+b_0L+b_1H} \\
x_B &= \frac{c_0+c_1L+c_2H+c_3L^2+c_4LH+c_5H^2}{1+d_0L+d_1H}
\end{aligned}
\tag{4.5}
$$

where $L = -ln(I_L/I_0)$ and $H = -ln(I_H/I_0)$. The parameters a_i, b_j, c_i, d_j $(i = 0{\sim}5, j = 0{,}1)$ can be experimentally determined and used for dual-energy imaging.

4.2.1.1.2 Basis Material Decomposition

Aluminum and acrylic were used as the basis material pair for this study, following the choices of early investigators [21, 62] in dual-energy CT. To determine the decomposition coefficients in Eqs. (4.5), an aluminum step-wedge and an acrylic step-wedge were machined and stacked in an orthogonal pattern, respectively, as shown in Figure 4-1(a). Projections were acquired with energy settings of 80 and 150 kVp. A typical projection image using 150 kVp is shown in Figure 4-1(b). For each row in the image, the measurement used the same thickness of aluminum but different thickness of acrylic. For each column in the image, the measurement used the same thickness of acrylic but different thickness of aluminum. For example, the ROI 1 in Figure 4-1(d) has a zero thickness of aluminum and 61.77 mm thickness of acrylic, and has corresponding L value of 1.61 and H value of 1.25. ROI 2 in Figure 4-1(d) has 49.44 mm thickness of aluminum and 61.77 mm thickness of acrylic, and has corresponding L value of 6.09 and H value of 3.80.

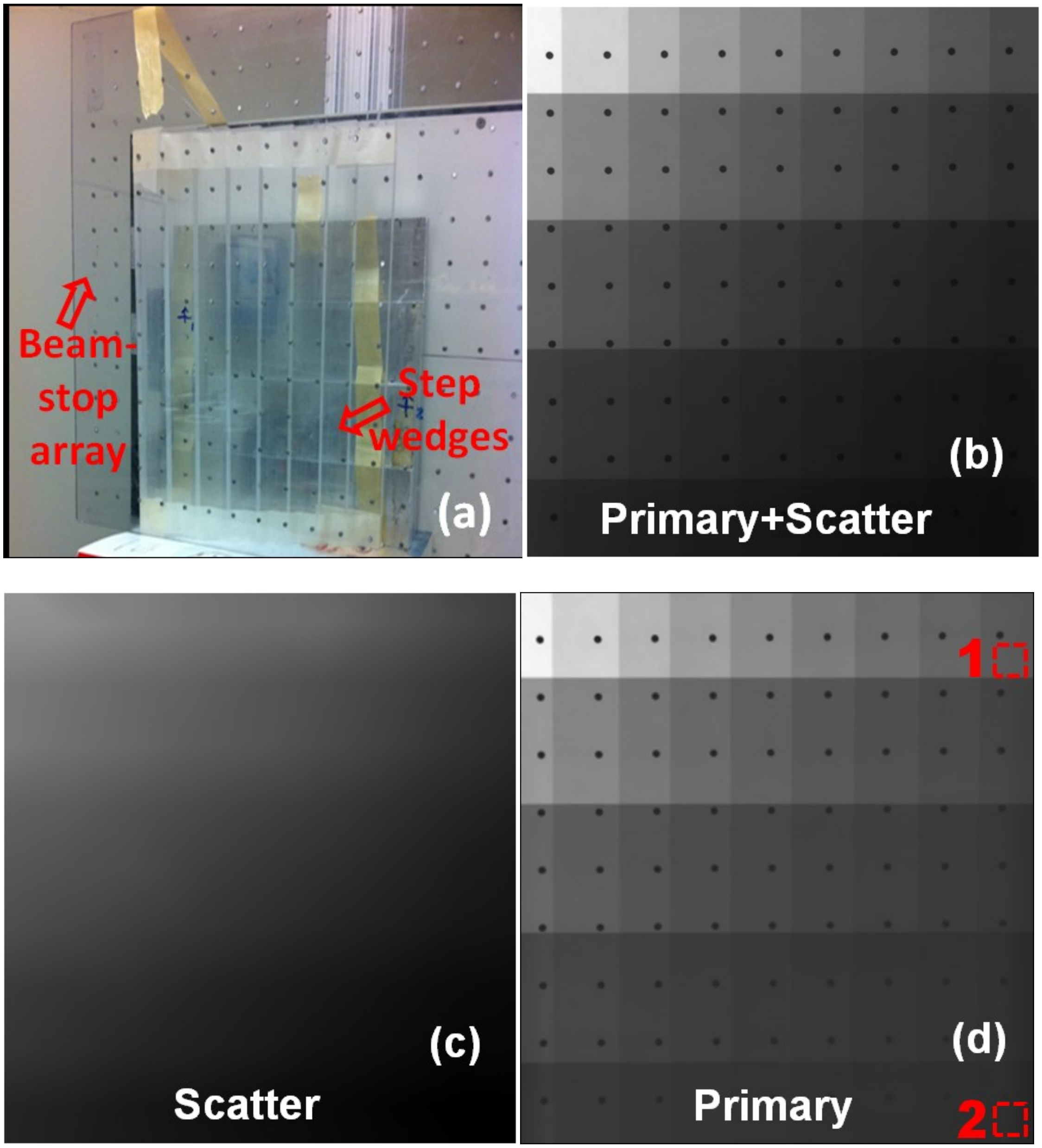

Figure 4-1 (a) Picture of the calibration step-wedges setup, (b) measured projection, (c) scatter estimation, and (d) corrected primary attenuation signal.

Scatter contributions were estimated using a beam-stop array set up in front of the step wedges, also shown in Figure 4-1(a), to provide point estimates of the scatter. In the beam-stop array, each beam-stop is made of 3 mm lead and at least 10 half-value layers for the incident beam. Therefore the majority of forward photons are effectively blocked and only the scattered photons reach the detector at those beam-stop spots. These point estimates were then linearly interpolated to provide a scatter map as shown in Figure 4-1(c). The scatter was subtracted from the measured projection data to generate the corrected data, as shown in Figure 4-1(d), for estimating parameters of a_i, b_j, c_i, d_j $(i = 0\sim5, j = 0,1)$. The whole parameterization process included 45 measurements for aluminum and acrylic. The parameters a_i, b_j, c_i, d_j $(i = 0\sim5, j = 0,1)$ for Eqs. (4.5) were estimated by minimum absolute error fitting, and they represent characteristics of the X-ray beam energy spectrum and are independent of the object being imaged.

After completing the aforementioned parameterization, the high and low energy projections were processed using Eqs. (4.5) on a pixel-by-pixel basis. The equivalent thicknesses of aluminum and acrylic (Eqs. (4.5)) could then be calculated. Two sets of basis material decomposed projections (aluminum and acrylic) were therefore generated from single energy (80 and 150 kVp) projections. In each set of decomposed projections, the pixel value is the equivalent thickness of basis material (aluminum or acrylic) components. The decomposed projections of aluminum and acrylic were then used to create synthesized monochromatic projections. A head phantom with a skull insert was used in our study to demonstrate the implementation of basis material decomposition, as shown in Figure 4-2(a).

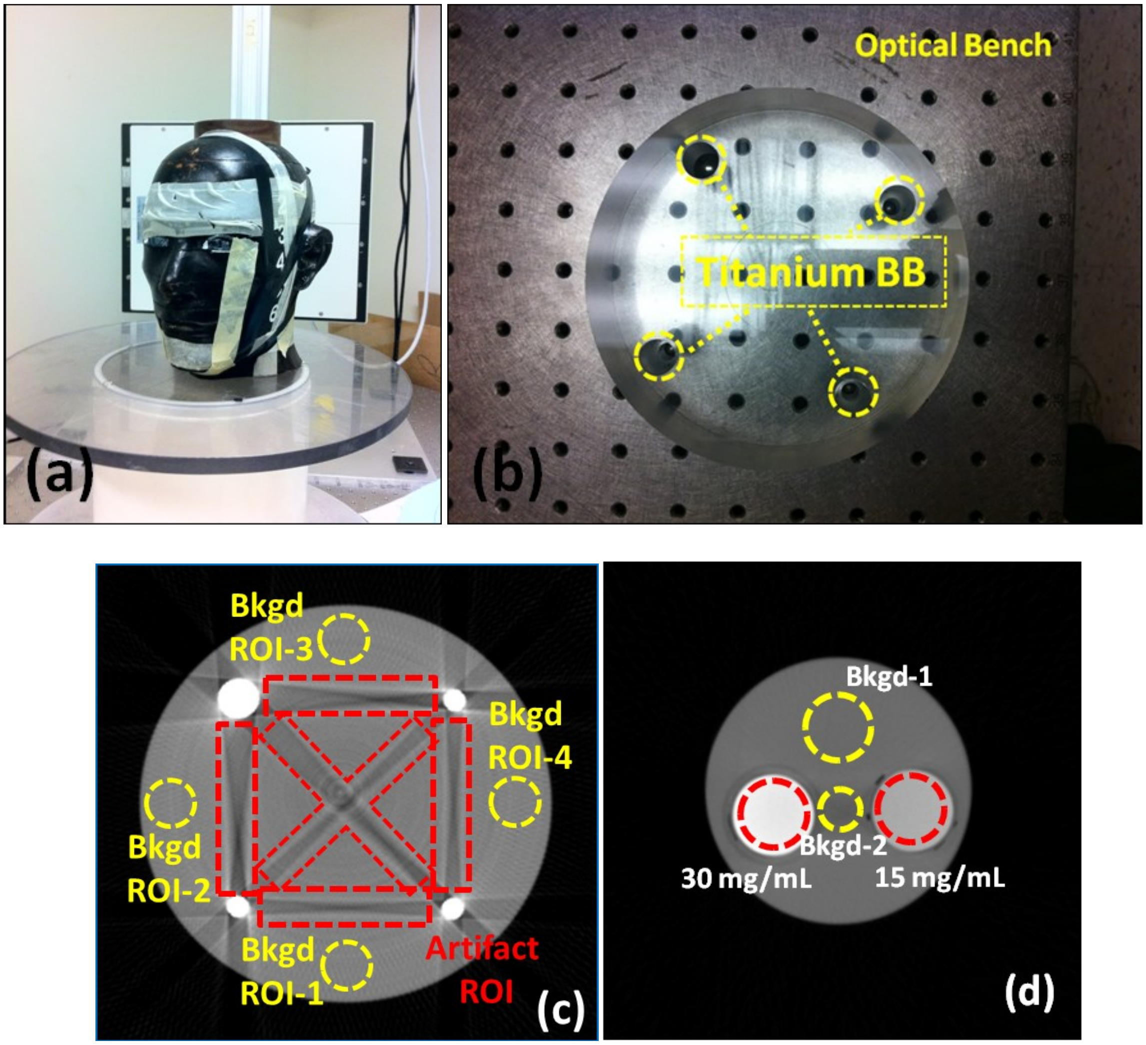

Figure 4-2 (a) The head phantom to demonstrate the basis material decomposition, and (b) the in-house titanium-BB phantom to demonstrate metal artifact reduction, (c) ROI selection for metal artifact reduction evaluation, and (d) ROI selection for optimal energy determination with two iodine concentrations.

4.2.1.2 Virtual Monochromatic CBCT

4.2.1.2.1 Theory

Mathematically, monochromatic projections can be synthesized after basis material decomposition utilizing the basis material attenuation coefficients for the selected monochromatic energy E_0 with x_A and x_B, where x_A and x_B are the equivalent thickness of basis materials A and B from the decomposed projections, respectively[20, 62]:

$$\int \mu(E_0)ds = x_A\mu_A(E_0) + x_B\mu_B(E_0) \qquad (4.6).$$

Since the monochromatic projections are synthesized as if they were acquired using a monochromatic X-ray source, the energy selection is referred to in units of keV in this chapter, e.g. 100 keV. In contrast, the single-energy CBCTs are acquired using polychromatic X-ray sources and the energy selection will be referred to in units of kVp in this chapter, e.g. 100 kVp.

4.2.1.2.2 Optimal Energy Selection for Metal-Artifact Reduction in Heavy Metal Objects

A cylindrical acrylic phantom with titanium-BBs was machined to mimic the metal artifact associated with dental implants, as shown in Figure 4-2(b). The scan dose for 125 kVp is about 1.2 cGy, while the dose for a 80 kVp and 150 kVp scan is 0.68 cGy and 0.60 cGy, respectively, totaling a dual-energy scan dose of 1.28 cGy. This indicates approximately 7% difference in the total dose between the dual-energy and single-energy CBCT scans. Therefore, the background noise measurement of the 125 kVp scan was adjusted by a factor of $\sqrt{1.28/1.2}$ to reflect this slight difference.

To quantitatively assess the performance of artifact removal, the standard deviation in the artifact ROI, shown as the area within the red dashed line in Figure 4-2(c), was calculated and compared between single-energy and LM CBCT. The background noise, calculated as the average standard deviation of four background ROIs, also shown in Figure 4-2(c), was compared between the single-energy and LM CBCT as well. The standard deviations for artifact and background ROIs were also studied as a function of VM energy selection to find the optimal VM energy.

4.2.1.2.3 Optimal Energy Selection for Iodine Contrast in Metal-Free Objects

An optimal monochromatic energy exists to maximize the CNR for certain material, e.g. iodine contrast, in metal-free objects in the VM CBCTs[66, 67]. To find this optimal energy for iodine contrast, two syringes, one with an iodine concentration of 15mg/mL and the other with 30mg/mL was placed in a water phantom to allow measurements of iodine signal within a water background. The phantom was then scanned at 80kVp and 150kVp (with additional tin filtration). VM CBCTs at 13 energies (30keV to 150keV, with 10keV intervals) were generated. The signal of each iodine concentration and the water background was measured, in addition to noise measurements of the water background, illustrated by the labeled ROI selections in Figure 4-2(d). The iodine CNRs for the two concentrations were then calculated based on contrast and noise measurements defined as:

$$CNR = \frac{|s_{Iodine} - s_B|}{\sigma_B} \tag{4.7}$$

where s_{Iodine} and s_B are the mean voxel values in the iodine ROI (15mg/mL or 30mg/mL) and background ROI-1 , respectively, and s_B is the standard deviation of background ROI-1 in Figure 4-2(d).

In theory, the beam hardening artifact is associated with the polychromatic characteristics of the X-ray beam and therefore should be removed in VM CBCT. To determine the optimal VM energy for beam hardening reduction, the absolute HU difference between the two background ROIs (1 and 2, also shown in Figure 4-2(d)) was calculated as a function of the VM energy.

4.2.2 Generation of Linearly Mixed CBCT

4.2.2.1 Optimal Weighting

Linearly mixed images were calculated using the following equation:

$$I_{Mix} = w_L I_L + w_H I_H \tag{4.8}$$

where I_L and I_H denote low- and high-energy CBCTs, respectively. w_L and w_H denote the weighting factors assigned to low- and high-energy images, which always satisfy $w_L + w_H = 1$.

If we define the standard deviation of the voxel values in the signal and background regions as $\sigma_{s,i}$ and $\sigma_{b,i}$, where the subscript $i = L, H$ denotes the low- and high-energy CBCTs, it has been shown that the weighting factor that minimized the background noise can be given by[68]:

$$w_L(\sigma_{min}) = \frac{\sigma_{b,H}^2}{\sigma_{b,H}^2 + \sigma_{b,L}^2} \qquad (4.9).$$

To maximize the CNR of a given ROI, the optimal weighting factor for the linearly mixed images is given by:

$$w_L(CNR_{max}) = \frac{C_L(\sigma_{s,H}^2+\sigma_{b,H}^2)}{C_L(\sigma_{s,H}^2+\sigma_{b,H}^2)+C_H(\sigma_{s,L}^2+\sigma_{b,L}^2)} \tag{4.10}$$,

where $C_i(i = L, H)$ is the contrast (voxel value difference) between the signal and background regions.

Under the optimal weighting factor for either noise minimization or CNR maximization, the image quality of the linearly mixed CBCTs is then dependent on total radiation dose and dose partitioning. Therefore, in this study, different dose partitioning schemes between the low- and high-energy scans were studied while the total imaging dose was kept equal.

4.2.2.2 Experimental Design

An electronic density phantom (Model 062, CIRS, Norfolk, VA) was used for the study as shown in Figure 4-3. For the dual-energy scan, the X-ray tube was operated at 150kVp, with additional tin filtration, and 80kVp without additional filtration. Single-energy scans of 80kVp, 100 kVp, 125kVp and 150kVp were acquired on an equal dose basis.

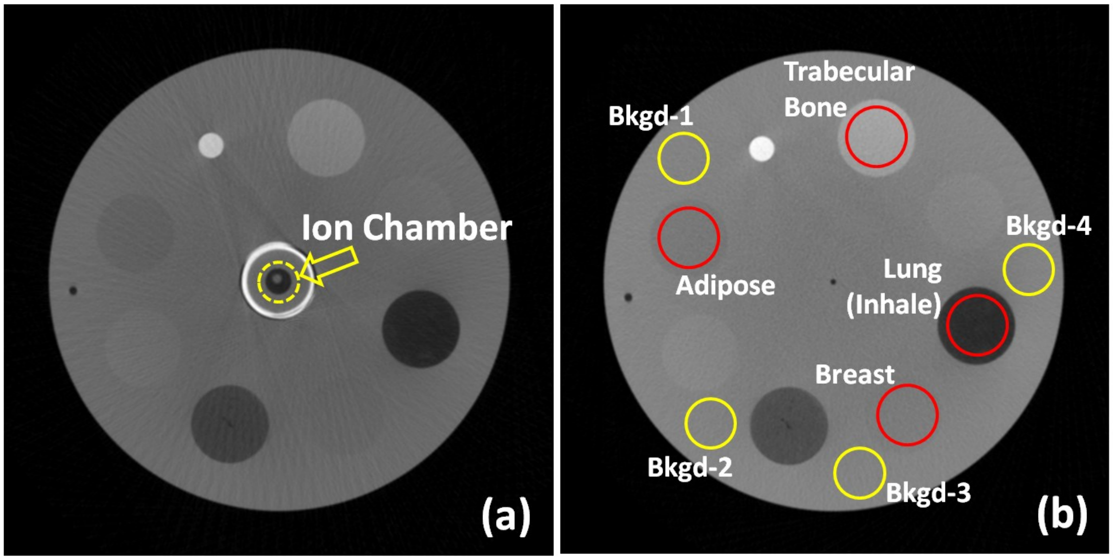

Figure 4-3 (a) Dose measurement using ion chamber, (b) ROI and background selection for CNR measurement

For the dual-energy study, different dose partitioning schemes between two energies (20%, 40%, 60% and 80% for 80kVp) were studied while the total dose was kept equivalent to the single-energy scans (80kVp, 100kVp, 125kVp and 150kVp). For each dose partitioning scheme and single-energy scan, the tube current (mA) and exposure time (ms) were adjusted such that each image was acquired on an equal dose basis. Because the generator offers a limited number of ms and mA settings, not all of the imaging doses were exactly the same. The dose for each image was verified with ion chamber measurements in the center of the phantom, as shown in Figure 4-3(a). To account for small differences in the imaging dose, the noise measurements were adjusted by the following factor: $\sqrt{(desired\ dose)/(measured\ dose)}$, which were 1.052, 1.052, 1.017 and 1.050 for 20%, 40%, 60% and 80% dose fractions at 80kVp, respectively.

The CNRs for different ROIs were calculated similarly to Eq. (4.7). The noise level was measured as the average of four background regions-of-interest (ROIs), as shown in Figure 4-3(b). The adipose and breast tissue inserts were selected as the low contrast objects for the CNR calculation, while the trabecular bone and lung (inhale) tissue inserts were representative of the high-contrast objects, also shown in Figure 4-3(b).

4.3 Results

4.3.1 Virtual Monochromatic CBCT

4.3.1.1 Basis Material Decomposition

The pre-reconstruction basis material decomposition for a head phantom is shown in Figure 4-4: the low- and high-energy projections (Figure 4-4(a) and (b)), as well as the aluminum and acrylic projections after basis material decomposition (Figure 4-4(c) and (d)). Note the substantial contrast differences between the projections in Figure 4-4(a, b) and (c, d), indicating the effectiveness of basis material decomposition.

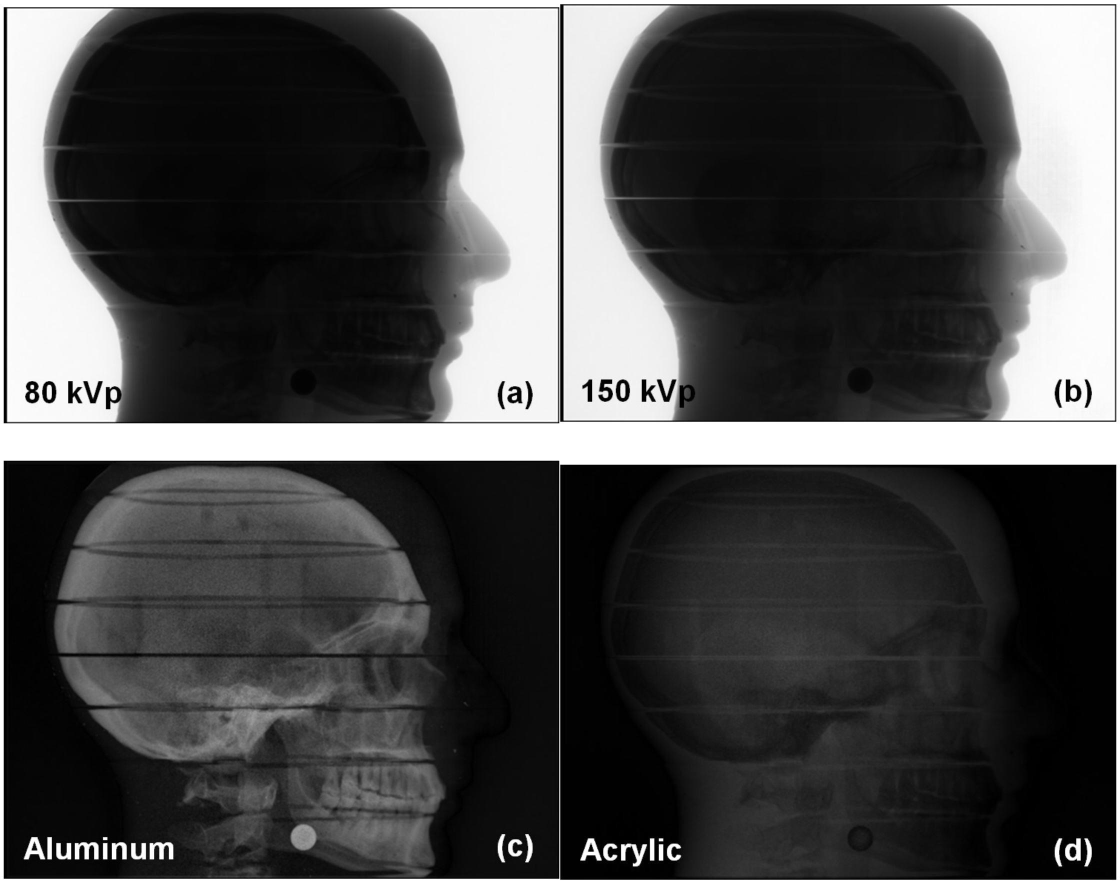

Figure 4-4 Prereconstruction basis material decomposition. Sample projections at the same rotational angle for (a) 80 kVp, (b) 150 kVp, (c) aluminum projection and (d) acrylic projection.

4.3.1.2 Virtual Monochromatic CBCT for Metal Artifact Reduction

The axial view of the reconstructed VM CBCTs is shown in Figure 4-5(b), and the corresponding axial view of the 125 kVp single-energy CBCT is shown in Figure 4-5(a). Note that the severe metal artifacts observed in Figure 4-5(a) are substantially reduced in the VM CBCT.

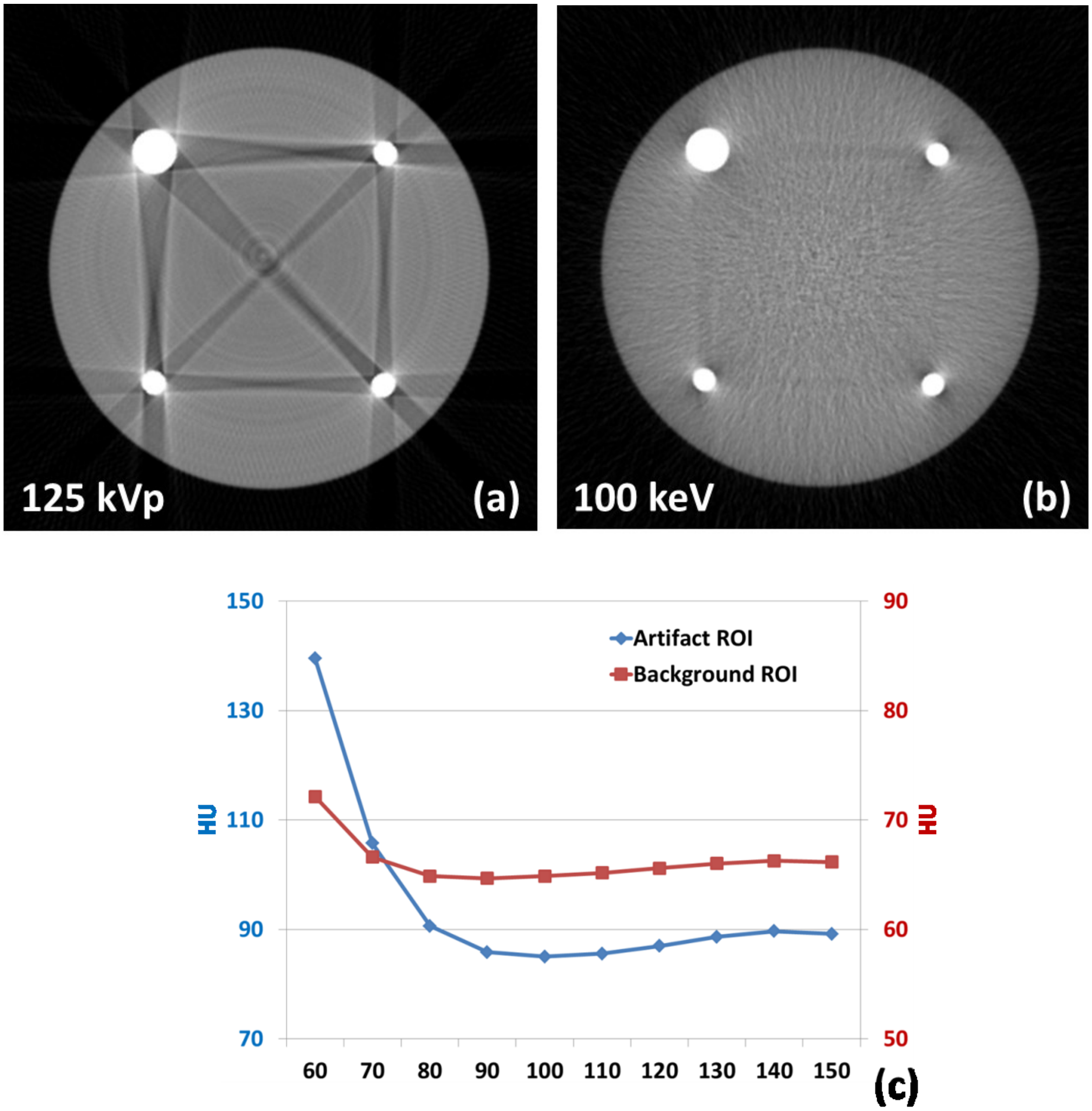

Figure 4-5 Axial CBCTs of titanium-BB phantom (window [-1000 1000]): (a) 125 kVp single-energy CBCT, (b) 100 keV VM CBCT, and (c) standard deviations for artifact and background ROIs at different VM energies.

The calculated standard deviations for the artifact ROIs from the 125 kVp single-energy CBCT and the 100 keV synthesized VM CBCT were 139 HU and 85 HU, respectively, which represents an approximately 40% reduction. However, the standard deviations in the background ROIs was 36 HU for the 125 kVp single-energy CBCT (after dose difference adjustment) in contrast with 65 HU for the 100 keV VM CBCT. Also, for the VM CBCT, the noise texture changed compared with the 125 kVp single-energy CBCT.

Standard deviations in the artifact ROIs and background ROIs of different VM energies ranging from 60 keV to 140 keV, were also calculated and plotted in Figure 4-5(c). The 100 keV VM energy minimized the standard deviation for the background ROI while 90 keV gave slightly better background noise performance (0.2 HU) when compared with 100 keV. Therefore, in the presence of heavy metal objects, 100 keV is the optimal VM energy to reduce metal artifacts.

4.3.1.3 Determination of Optimal VM Energy for Metal-Free Objects

The VM CBCTs reconstructed from a range of VM energies between 30keV and 150keV and single energy CBCTs (80kVp and 150kVp) for the water phantom with two iodine concentrations are shown in Figure 4-6(a). The iodine CNRs at various VM energies are plotted in Figure 4-6(b). The maximum iodine CNR is achieved for a VM energy of 50keV for both iodine concentrations. The beam hardening artifact reaches a minimum at 60 keV for the iodine phantom study, as shown in Figure 4-6(c).

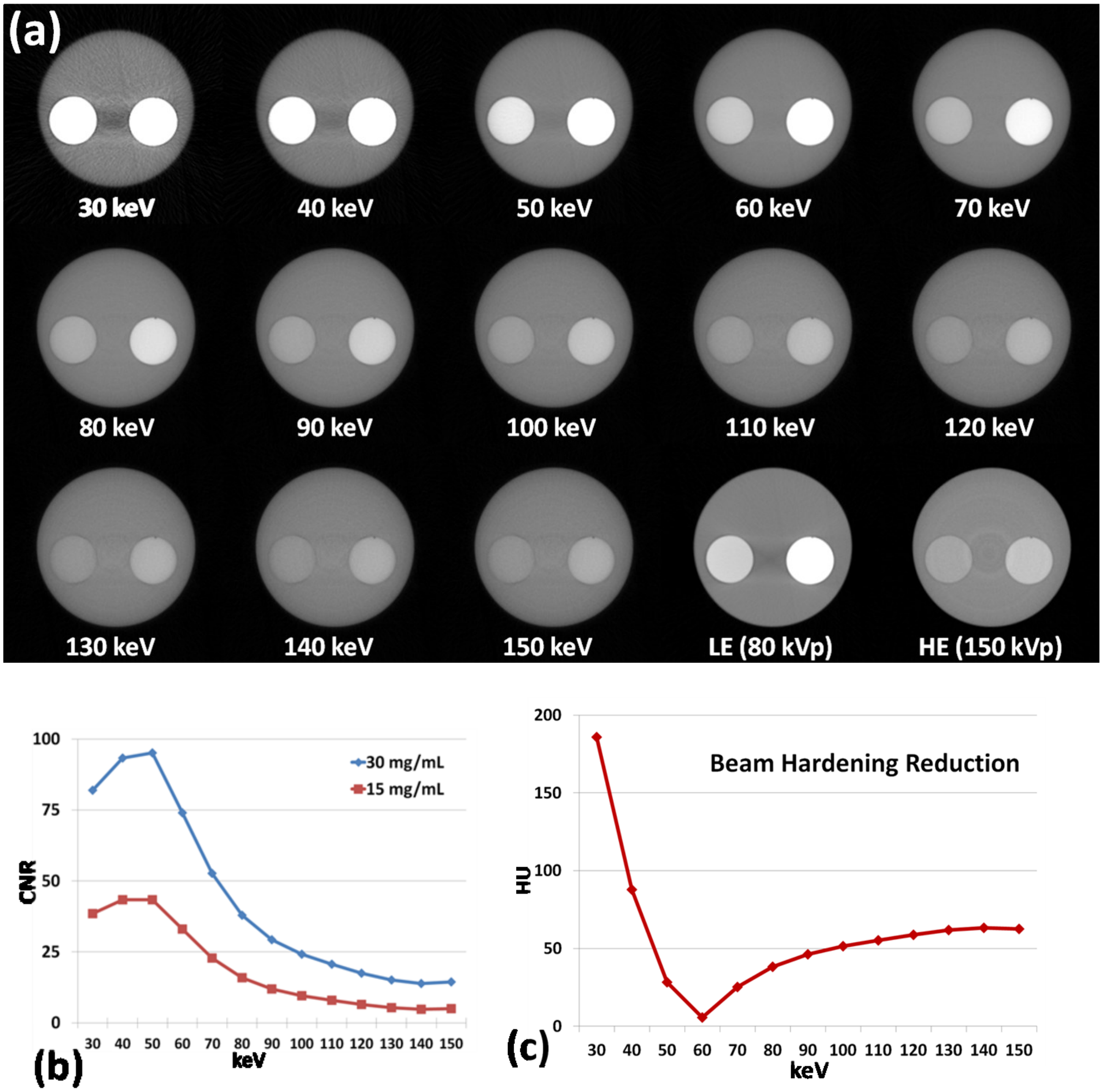

Figure 4-6 (a)VM CBCTs of the water phantom containing two iodine concentrations at different VM energies: 30-150 keV, and low-(80 kVp) and high-energy (150kVp) CBCT (window [-1000 1000]), (b) CNRs for two iodine concentrations at different VM energies, (c) beam hardening reduction at different VM energies.

4.3.2 Linearly Mixed CBCT

The single-energy CBCTs at different energies and LM CBCTs with different dose fractions with the same total dose are shown in Figure 4-7. It can be seen that as the dose fraction increases for the low-energy scan (e.g. Figure 4-7(e)), the contrast in the LM CBCT increases, when compared with a lower dose fraction for the low-energy scan(e.g. Figure 4-7(h)).

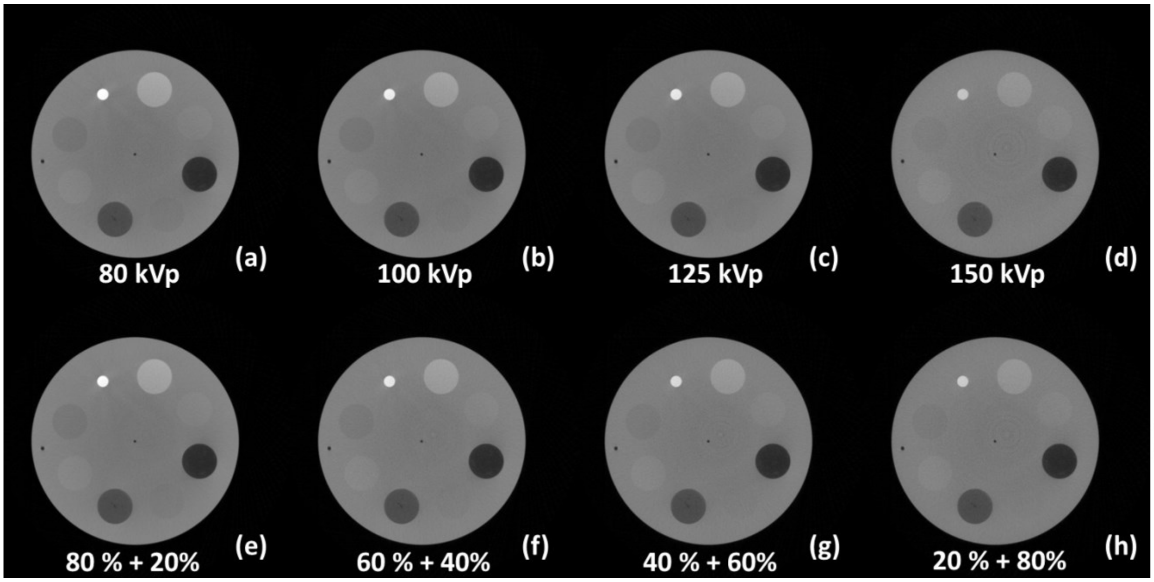

Figure 4-7 Single-energy CBCTs at: (a)80kVp, (b)100kVp, (c)125kVp and (d)150kVp; LM CBCTs with different dose fractions: (e) 80% low-energy and 20% high-energy, (f) 60% low-energy and 40% high-energy, (g) 40% low-energy and 60% high-energy, and (h) 20% low-energy and 80% high-energy. Window: [-1000 1000].

4.3.2.1 Noise

For each CBCT data set with different dose partitioning scheme at 80 kVp, the optimal linearly mixing weighting factor was determined using Eq. (4.9). The dose fractions assigned for an energy of 80 kVp for the dual energy scans were 20%, 40%, 60%

and 80%. The noise levels in dual-energy CBCT linearly mixed images are compared with those from the single-energy CBCTs for the same total radiation dose and are shown in Figure 4-8(a). The noise in the linearly mixed image in Figure 4-8(a) is comparable to that of single-energy CBCT scans. The difference in average noise level between the dual-energy LM CBCTs and the equivalent-dose single-energy CBCTs was measured to be 1.2% in the phantom background.

4.3.2.2 Contrast-to-Noise Ratio

For each data set with different dose fractions at 80 kVp and for different ROIs, the optimal weighting factors to maximize CNR were calculated using Eq. (4.10). Figure 4-8(b) and (c) show variations of the maximal CNRs in the LM CBCTs in comparison to those of the single-energy CBCTs for approximately the same total radiation dose level for both low-contrast and high contrast objects, respectively. For four tissue types (trabecular bone, lung, adipose and breast), CNR values in the LM CBCTs using any dose partitioning scheme are better than those of the 150 kVp single-energy CBCTs. The average CNR for the four tissue types with a 80% dose fraction at low-energy showed 9.0% and 4.1% improvement relative to the 100 kVp and 125 kVp single-energy CBCTs, respectively. CNRs for low contrast objects improved as the dose fraction was increased towards the low-energy component (80kVp) for the LM CBCTs.

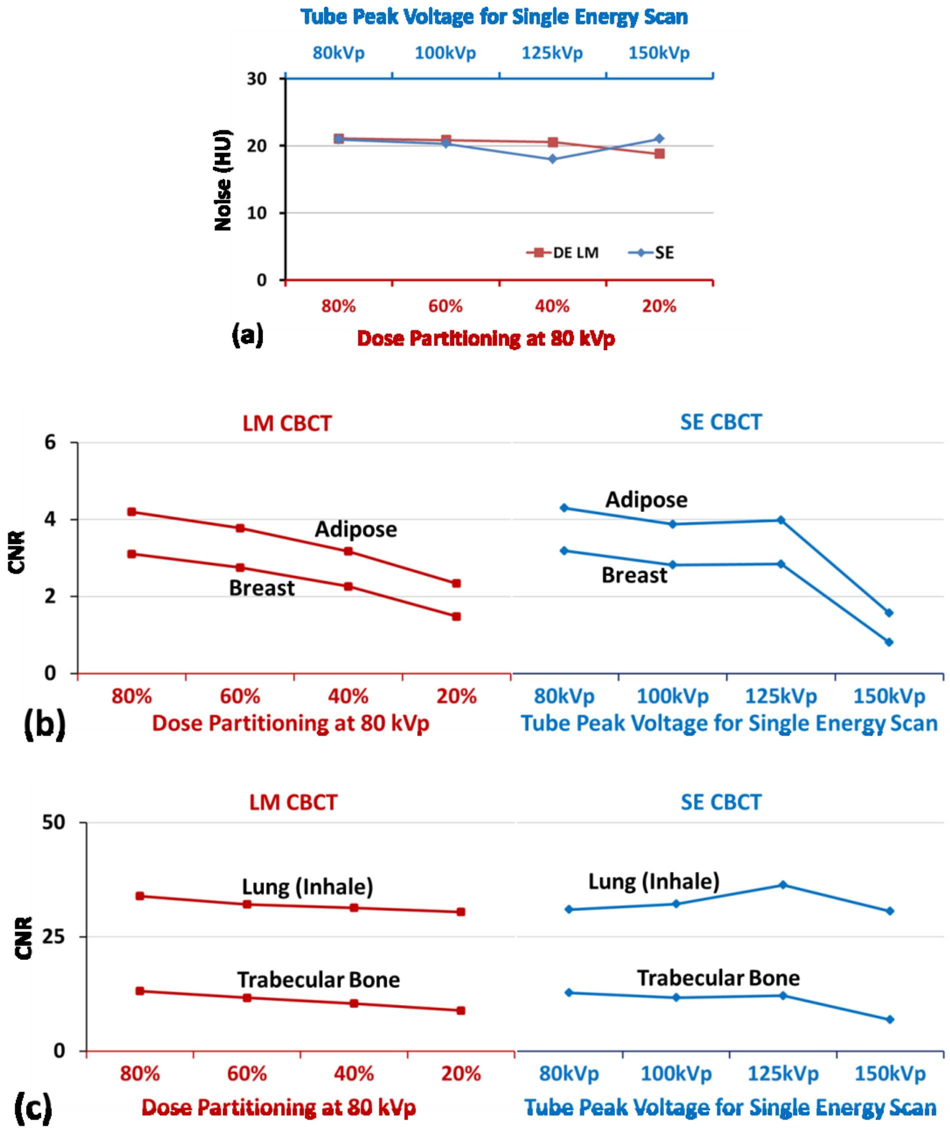

Figure 4-8 (a) Minimum noise, and (b,c) maximum CNR in linearly mixed dual-energy CBCTs for various dose partitioning compared with those of single-energy CBCTs with equivalent dose level. The minimum noise and maximum CNR for each tissue was obtained using the optimal weighting factor from Eq. (4.9) and (4.10), respectively, to form the linearly mixed dual-energy CBCTs.

4.4 Discussion

We have demonstrated the successful basis material decomposition for dual-energy CBCT. Metal artifact reduction is just one of many applications for dual-energy

CBCT in radiation therapy. Other advanced techniques[61, 69] can be applied in combination with the VM technique to further improve the effectiveness of metal artifact reduction. Bamberg et al.[61] proposed a patient study using monoenergetic extrapolation for metal artifact reduction in dual energy CT while Xue et al.[69] proposed another metal artifact reduction technique in dual-energy CT using active contour modeling and TV inpainting. In addition to metal artifact reduction, the information gathered from pre-reconstruction basis material decomposition for the VM technique provides anatomical information that is usually not remarkable in single energy projections (e.g. tissue characterization of tumors). The anatomical information provided by basis material decomposition has been demonstrated to be of diagnostic value in dual-energy CT[12, 70, 71]. This information can be potentially utilized for target localization during radiation therapy using both 2D and 3D techniques. Other studies have reported that noise in the basis material decomposed images was negatively correlated and could be used for noise reduction in the images[72]. A noise reduction by factors of 2 to 5 was achievable in phantom experiments and clinical examples by Kalender et al.[72].

In principle, the monochromatic CBCTs should be free of beam-hardening artifacts. However, it is practically impossible to obtain ideal monochromatic images due to X-ray scatter and decomposition error. Therefore, some artifacts in the area surrounding the titanium-BBs can still be observed in the VM CBCT as shown in Figure 4-5(b).

The selection of the optimal energy E_0, for the synthesized VM CBCT can have a large impact on the CBCT image quality. Both the mass attenuation coefficient and contrast decrease with increased energy. According to a study done by Wu et al.[67], the noise of the VM CT was higher when a greater or lower E_0 value was selected and there existed an optimal energy at which low contrast detectability and noise performance were favorable. For the phantom study with heavy metal artifacts, the projections suffered substantial attenuation from photons passing through the metal. For metal-free objects, such as soft tissues, the photon attenuation is substantially less. The optimal VM energy for metal artifact reduction was found to be around 100 keV while the optimal VM energy for iodine was only 50 keV. Therefore, the optimal VM energy selection used for metal artifact reduction is different from that for metal-free objects. For metal-free objects, optimal VM energy selection will also depend on the tissue of interest[66, 73].

Fractional polynomials (Eqs. (4.5)) were used in this study[65] to directly approximate the basis material decomposition shown in Figure 4-4. The method is simple, effective and still used in many recent studies[74, 75]. Because the values of the fractional polynomial increase monotonically in an asymptotic pattern from zero near the origin to infinity for large values, this function is well-defined (with the exception of negative L and H values which do not have any physical meaning). This results in a robust algorithm in the presence of the noise[65]. Also, because the fitted function has a smooth and monotonic surface, it can be reliably extrapolated well beyond the parameterization region, with limited loss of accuracy, while avoiding artifacts for thick patients and bony regions[65]. Iterative techniques[76] can be used to further improve the accuracy of the basis material decomposition.

Basis material decomposition can be used to differentiate materials and determine material-specific information. Conversely, the LM technique can create non-material-specific images. By linearly combining low- and high-energy CBCTs with optimal weighting factors, good quality of LM CBCT could potentially be used for routine patient setup and target localization. Therefore, dual-energy scans can be used to generate LM CBCT, and at the same time provide material-specific information for metal artifact reduction in VM CBCT. The optimal weighting factors calculated using Eqs. (4.9) and (3.10) for LM CBCT depend on the contrast and noise level of low- and high-energy CBCTs, and thus depend on tissue types and dose partitioning. Using these optimal weighting factors, this study has demonstrated that the LM CBCTs could achieve similar noise and CNR relative to the typical single-energy CBCTs for a wide range of tissue types (lung, trabecular bone, adipose, and breast). The LM CBCT could potentially be used to improve the image quality when increasing the dose fraction for low-energy (80 kVp) projection acquisition. One limiting factor when using dual-energy imaging for both VM and LM CBCT is that basis material decomposition requires comparable noise levels between the low- and high-energy projections. Dose fractions assigned to low energy projections should not deviate significantly from 50% in clinical practice, in order to ensure similar noise levels between low- and high-energy projections. Therefore, dual-energy imaging may not be able to achieve both goals at the same time.

Since the same object is scanned twice in dual-energy CBCTs, the scan dose can be potentially greater than that of a single-energy CBCTs. Thus, one important question that needs to be addressed is: how does the image quality of dual-energy CBCTs compare with single-energy CBCTs at equivalent radiation dose levels? Intuitively, low energy scans usually provide images with good contrast but often suffer from increased noise due to the physics of greater photon absorption at lower energies. Conversely, high energy scans provide lower contrast but better noise properties. Image quality for LM CT images has been previously analyzed[68] but it remains unclear as to how LM CBCTs perform when compared to single-energy CBCTs under the same radiation dose. By linearly combining low- and high-energy CBCTs, the mixed images can potentially benefit from both ends when it comes to dual-energy imaging.

4.5 Conclusions

We implemented the dual-energy technique for virtual monochromatic and linearly mixed CBCT. Virtual monochromatic CBCT can be used for metal artifact reduction, while linearly mixed CBCT can provide similar image quality in terms of noise and CNR when compared with single-energy CBCT acquired with equivalent dose. This indicates that under the same total imaging dose the dual-energy CBCT scan has the potential to improve imaging performance such as metal artifact reduction when compared to single-energy CBCT.

5. Development of an Aggregated kV/MV Imaging Technique

5.1 Motivation

KV radiography and kV CBCT have proven to be powerful tools for improving localization accuracy in the treatment room with image-guided radiation therapy[18, 33]. MV radiography and MV CBCT has the potential to provide complimentary advantages when compared to kV imaging[34-36]. First, MV beams are less attenuated and therefore more suitable for penetrating through larger objects. Second, MV imaging usually suffers less from metal artifacts caused by dental implants or hip prostheses. Therefore, an aggregated CBCT system that combines both kV and MV projections may provide better image quality over a system using only kV or only MV projections.

Moreover, the data acquisition efficiency could be improved by acquiring kV and MV projections using an aggregated kV/MV scheme. Modern linear accelerators are typically equipped with both kV and MV imaging devices mounted on the gantry. By using an aggregated kV/MV acquisition scheme, the gantry only needs to rotate around 110° to acquire sufficient data for CBCT reconstruction, thus reducing the rotation time by approximately a factor of 2.

To generate meaningful aggregated CBCT images, a suitable scheme to combine kV and MV projections must be accomplished. Yin et al. [47] and Zhang et al. [48] proposed a linear gray scale conversion transformation by overlapping projections from a 10° interval for kV and MV beams. Blessing et al. [49] and Wertz et al. [50] mapped MV projections to kV projections by histogram adaptation. These methods are convenient to implement in kV/MV imaging. However, using these methods, the aggregated image quality is sensitive to the selected mapping technique between kV and MV information, which was based on the gray level of projections.

In this chapter, the traditional dual-energy imaging technique used in diagnostic imaging was extended to reconstruct dual energy images with kV and MV energy sources. Specifically, the virtual monochromatic (VM) technique was adapted to provide the flexibility to reconstruct VM CBCT with a user selected VM energy for potentially improving contrast performance and for suppressing streaking artifacts that are mainly associated with the polychromatic nature of X-ray beams. The effectiveness of these techniques was evaluated and demonstrated using phantom studies. When testing the effectiveness of the technique, it is important to note that the deeply penetrating MV beams provide better noise performance at the cost of a reduction in imaging contrast. Therefore, CNR was utilized as one of major criteria to balance these two competing factors.

5.2 Methods

5.2.1 Theory

In the diagnostic energy range, the attenuation coefficients of biological tissues can be approximated by a linear combination of two basis materials[77]. Conventionally, a tissue-like material such as acrylic and a bone-like material such as aluminum are chosen as the basis materials. For a monochromatic source with energy E_0, the attenuation along a ray can be written as a linear combination of these two basis materials acrylic and aluminum for an incident radiation I_0 and an exit radiation I as [62, 64]:

$$ln(I/I_0\ ) = -\mu_{acrylic}(E_0)x_{acrylic} - \mu_{Al}(E_0)x_{Al} \tag{5.1}$$

where $x_{acrylic}$, x_{Al} and $\mu_{acrylic}(E_0)$, $\mu_{Al}(E_0)$ represent the equivalent composition material thickness (mm) and the linear attenuation coefficients (mm-1), of the object along the ray, respectively.

For large object thickness with energy E lower than 17 MeV, the attenuation behaves asymptotically in a linear fashion and can be approximated as [65]:

$$ln(I/I_0\ ){\sim} - \mu_{acrylic}(E_p)x_{acrylic} - \mu_{Al}(E_p)x_{Al} \tag{5.2}$$

where E_p is the peak energy of the polychromatic spectrum. As a good approximation, it is thus possible to extend the application of Eq. (5.1) given for the diagnostic energy range to the MV range.

For the polychromatic kV and MV projections with spectra $S_{kV}(E)$ and $S_{MV}(E)$, the measurements I_{kV} and I_{MV} are as follows [8-9]:

$$\begin{cases} ln(I_{kV}/I_0) = \int S_{kV}(E)\left[-x_{acrylic}\mu_{acrylic}(E) - x_{Al}\mu_{Al}(E)\right]dE \\ ln(I_{MV}/I_0) = \int S_{MV}(E)\left[-x_{acrylic}\mu_{acrylic}(E) - x_{Al}\mu_{Al}(E)\right]dE \end{cases} \tag{5.3}$$

According to Cardinal et al. [65], approximation of the acrylic and aluminum composition of the material can be found using the following equations for Eqs. (5.3):

$$x_{acrylic} = \frac{a_0+a_1L+a_2H+a_3L^2+a_4LH+a_5H^2}{1+b_0L+b_1H}$$
$$x_{Al} = \frac{c_0+c_1L+c_2H+c_3L^2+c_4LH+c_5H^2}{1+d_0L+d_1H} \quad (5.4)$$

where $L = -\ln(I_{kV}/I_0)$ and $H = -\ln(I_{MV}/I_0)$. The parameters a_i, b_j, c_i, d_j ($i = 0{\sim}5, j = 0{,}1$) can be experimentally determined and used for kV/MV imaging.

Mathematically, virtual monochromatic (VM) projections can be synthesized after basis material decomposition utilizing the basis material attenuation coefficients at the selected monochromatic energy E_0 with $x_{acrylic}$ and x_{Al} [20, 62]:

$$\int \mu(E_0)ds = x_{acrylic}\mu_{acrylic}(E_0) + x_{Al}\mu_{Al}(E_0) \quad (5.5).$$

The attenuation coefficients used in the study were found in the National Institute of Standards and Technology (NIST) database.

Since the monochromatic projections are synthesized as if they were acquired using a monochromatic X-ray source, the energy selection is labeled with the units of keV or MeV, e.g. 100keV, 2MeV. In contrast, the kV and MV CBCTs are acquired using polychromatic X-ray sources and the energy selection will be labeled with the units of peak energy kV or MV, e.g. 125kV, 4MV.

5.2.2 Imaging System

The kV and MV projections were acquired on a Varian TrueBeam machine in Developer Mode (Varian Medical Systems, Palo Alto, CA). In Developer Mode, TrueBeam enables access to additional control features (compared to Clinical Mode), and is driven between control points coded in extensible markup language (XML). XML programming allows Developer Mode users to implement complex beam deliveries to perform experiments. In this study, user-designed XML beams were delivered for both kV and MV imaging.

Both the kV and MV detectors had the same physical size of 40x30cm^2 and were the centrally aligned with the gantry isocenter. The MV X-ray jaws were set to 26.5x20cm^2, which corresponds to two thirds of the detector size at the gantry isocenter position. The resolution of the kV and MV detector was 2048x1536 and 1024x768 pixels, respectively. The exported kV and MV projections were downsampled to 512x384 for reconstruction so as to be comparable to clinical data pre-processing of on-board CBCT. An FDK type[44] algorithm was used to reconstruct all CBCTs.

5.2.3 General Scheme

To determine the decomposition coefficients in Eqs. (5.4), an aluminum step-wedge and an acrylic step-wedge were stacked in an orthogonal pattern to provide different thickness combinations. The wedge set-ups for MV and kV beam projections are shown in Figure 5-1(a). Projections for the stacked step-wedges were acquired with a kV setting of 125 kVp and an MV setting of 4 MV. This setting is used for all of the experiments in this study unless otherwise specified. The whole parameterization process included 45 measurements for aluminum and acrylic. The parameters a_i, b_j, c_i, d_j $(i = 0\sim 5, j = 0,1)$ for Eqs. (5.4) were generated through data fitting based on minimum absolute error, and these parameters represent the characteristics of the kV and MV beams, as shown in Figure 5-1(b).

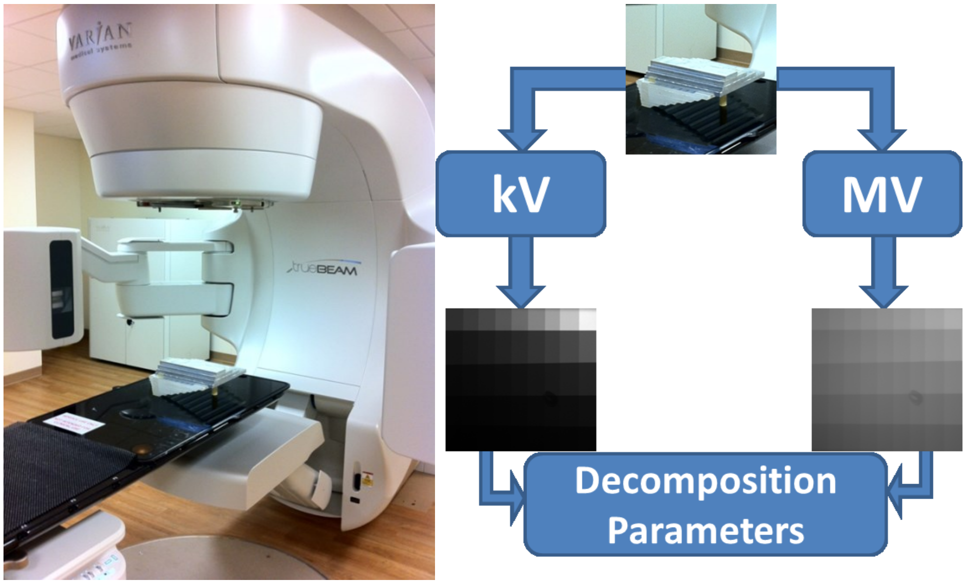

(a) **(b)**

Figure 5-1 Experimental determination of parameters to characterize kV and MV beams to synthesize VM projections from the treatment machine: (a) step-wedge set up on the treatment couch, (b) parameterization of Eq. (5.4).

With the current orthogonal kV/MV imaging hardware for modern linear accelerators, both MV projections (from gantry angle of 0° to 90°, up to 100°) and kV projections (90° to 200°) were acquired as the gantry rotated 110°, as illustrated in Figure 5-2.

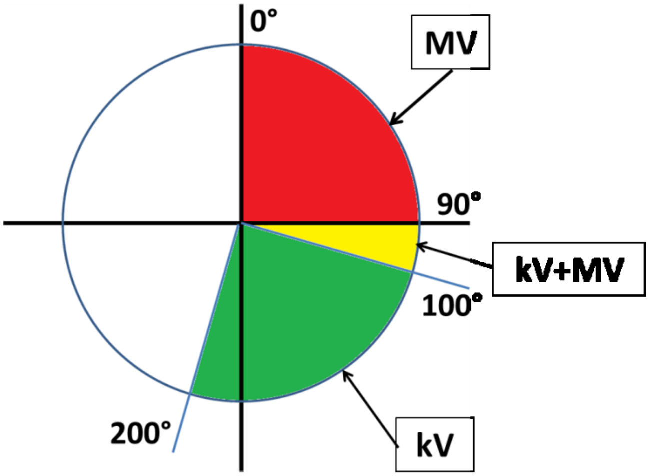

Figure 5-2 Acquisition scheme: kV and MV coverage. MV covers up to 100° (red), kV covers 110° (green), kV and MV has up to 10° overlap (yellow).

Some overlap projections (selected from 1 up to 10) between 90° to 100° were then decomposed into aluminum and acrylic material projections using the parameters previously determined. Two sets of material decomposed projections were therefore generated from kV and MV projections. In each set of decomposed projections, the pixel value could be viewed as the equivalent thickness of the material (aluminum or acrylic). Given the attenuation coefficients of aluminum and acrylic at a predetermined energy, one VM projection can be synthesized from two corresponding decomposed projections. The whole workflow of VM projection generation is shown in Figure 5-3.

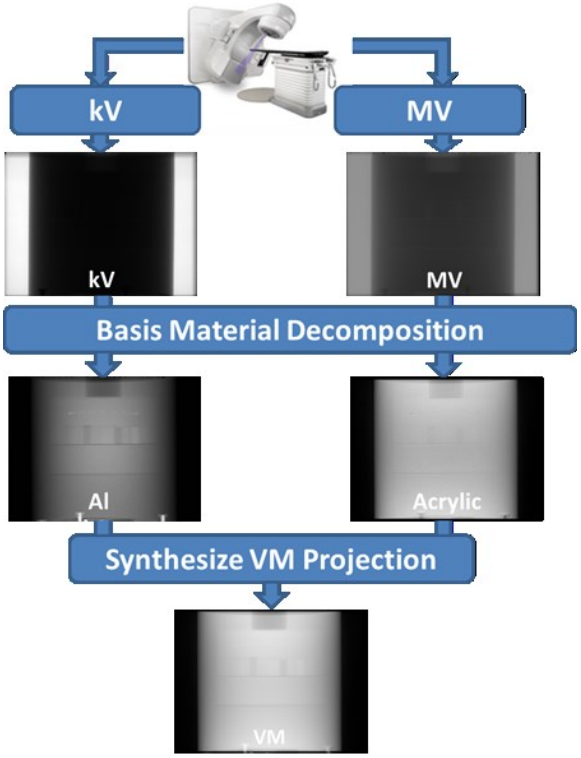

Figure 5-3 Synthesis of VM projections from kV and MV projections. Two basis material projections are firstly decomposed from kV and MV projections, VM projections are then synthesized at a selected energy.

Two linear functions were generated by fitting pixel values of kV and MV projections at these overlap angles (90° to 100°) to those of VM projections at the non bare-beam region, as shown in Figure 5-4. At non-overlap angles, kV and MV projections are first pre-processed using a log conversion to obtain attenuation coefficients for each pixel. Then using the fitted functions, kV and MV projections at other angles were linearly converted to approximate VM projection data covering 200°, as shown in Figure 5-5. VM CBCTs at a pre-specified energy were reconstructed from these converted projections, enough for a coverage of 180° plus the fan-angle of 15.2°.

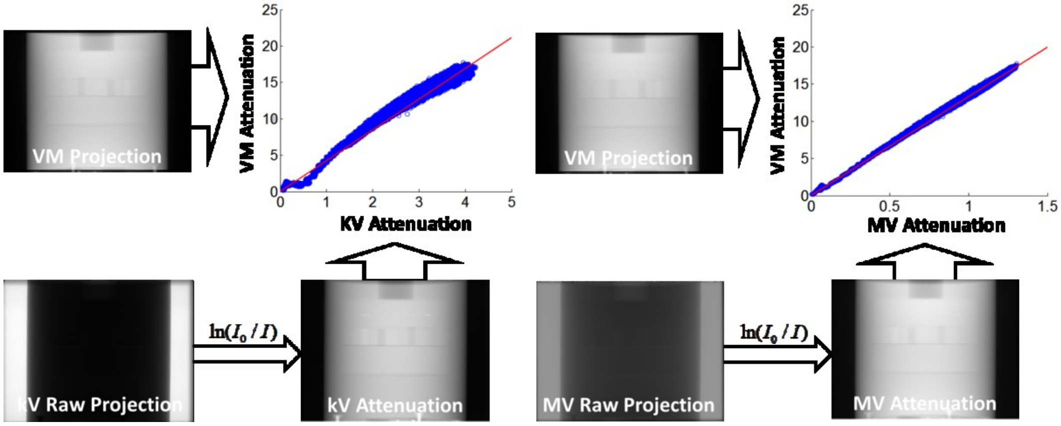

(a) **(b)**

Figure 5-4 Linear conversion functions for (a) kV, and (b) MV projections into compatible VM projections.

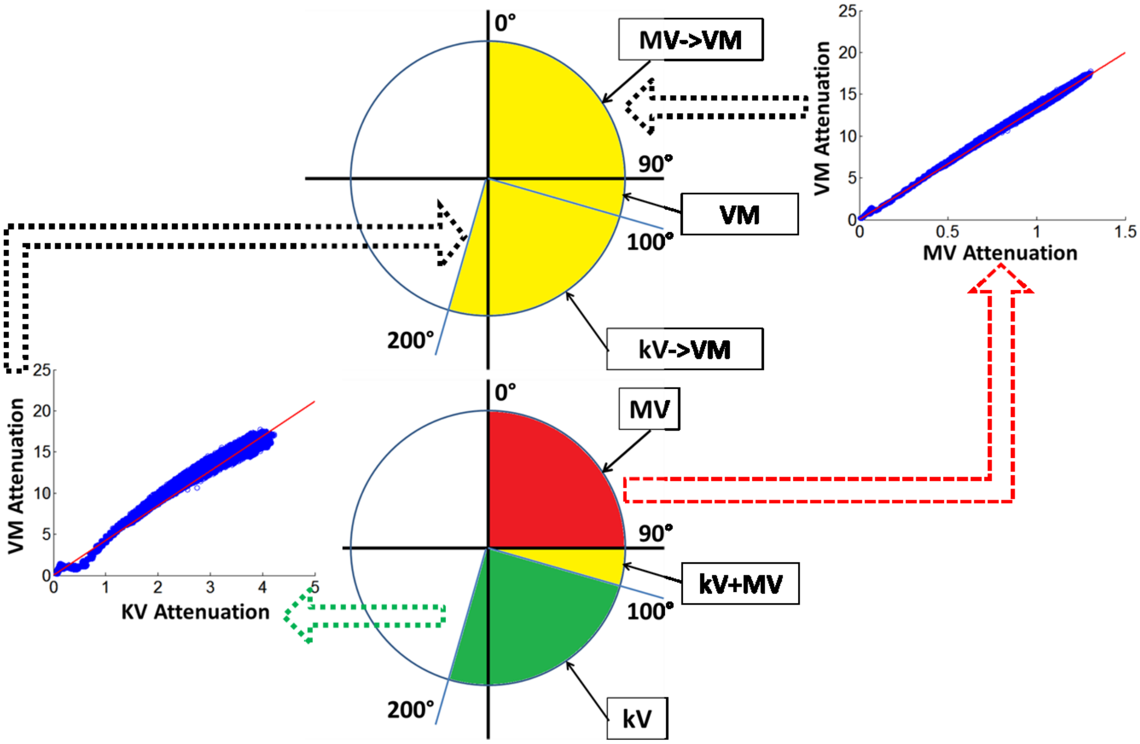

Figure 5-5 Generation of compatible VM projections covering reconstruction angles. MV projections (red) and kV projections (green) are linearly converted to approximate VM projections at these non-overlap angles using the linear conversion function generated in Figure 5-4.

5.2.4 Evaluation

5.2.4.1 Effect of virtual monochromatic energy

The contrast-to-noise ratios (CNRs) were calculated for different inserts in VM CBCTs of a CatPhan phantom with various selected energies and compared with those in kV and MV CBCTs. The selection of the regions-of-interest (ROIs) for the different inserts is shown in Figure 5-6. Only a one degree overlap angle was used to generate the linear fitting function in II.C. Thus, a total of 91 MV projections and 110 kV projections were acquired for reconstruction and 200 VM projections were then generated using the aforementioned conversion described in Section 5.2.3.

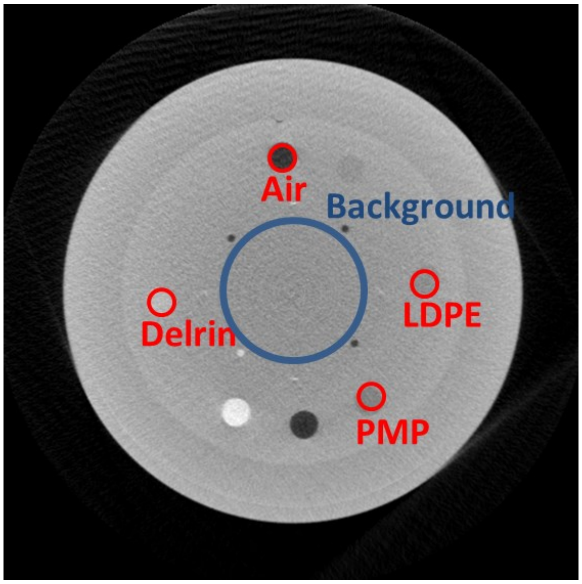

Figure 5-6 ROI selection for CNR evaluation.

5.2.4.2 Effect of overlap projections

The effect of the kV/MV overlap size was also studied using the CatPhan and ROI selection described in Figure 5-6. Three different numbers of overlap projections (1, 5, and 10) were used to generate the linear fitting function. Thus 91, 95 and 100 MV projections were acquired for the 1, 5, and 10 overlap scenarios.

5.2.4.3 Effect of beam orientation

To study the impact of the beam orientations on the image quality, we scanned the CatPhan with two pieces of 5cm thick solid water attached on both lateral sides of the phantom, as shown in Figure 5-7(a). Twelve different starting angles were selected, from 0° to 330° with a 30° interval, as labeled in Figure 5-7(b). The gantry was rotating counterclockwise during the scan. CNR was calculated for two ROIs as a function of beam orientation for the twelve angles.

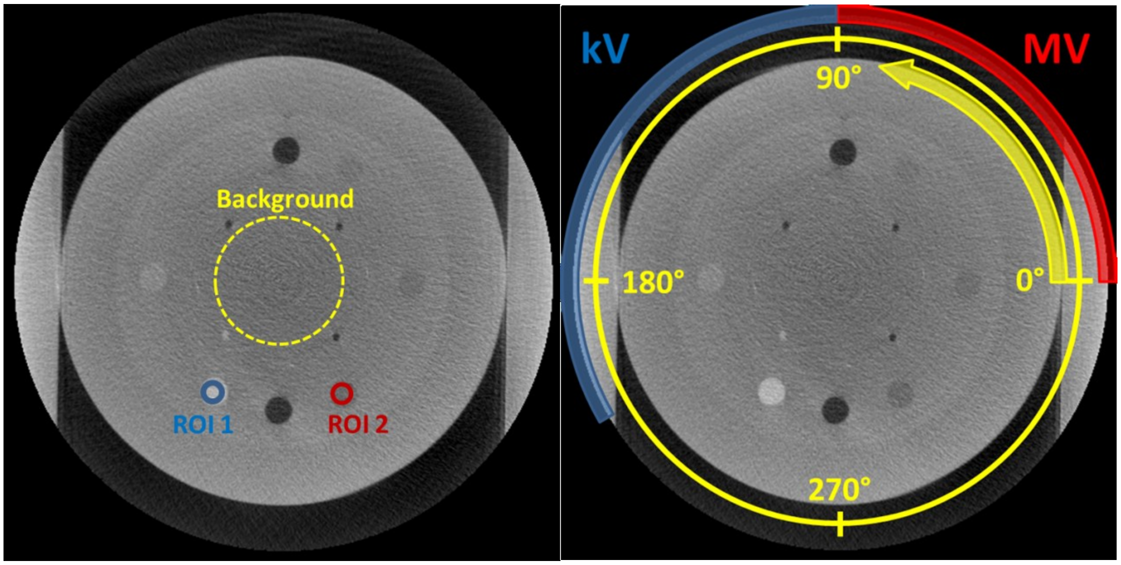

(a) **(b)**

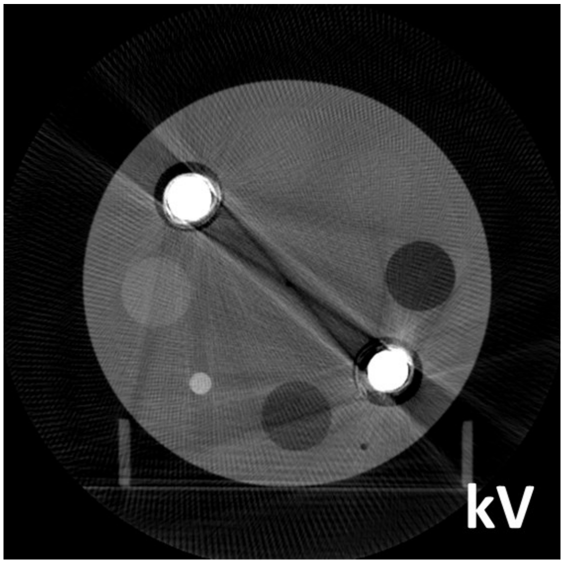

(c)

Figure 5-7 (a) ROI selection for the beam orientation study, (b) definition of starting angle, (c) kV CBCT of the electronic density phantom with two bolts inserted.

We also studied the impact of beam orientation on the image quality for objects with metal implants. Two bolts were inserted into an electronic density phantom to create severe streak artifacts, as shown in Figure 5-7(c). One kV CBCT, one MV CBCT and two different kV/MV beam orientations were applied to study the effect of beam orientation on metal artifacts.

5.2.4.4 Effect of iterative reconstruction

To lower the number of projections needed, we used a simultaneous algebraic reconstruction techniques (SART) based method [78] for the VM CBCT reconstruction. Four different sets of projections, 100, 67, 40 and 20, were used for the evaluation. These four sets used only one half, one third, one fifth, and one tenth of the total projections under the original experiment set-up but covered the same angular range.

5.3 Results

5.3.1 VM CBCT Reconstruction

Examples of VM CBCT axial slices at selected energies (30keV, 40keV, 50 keV, 100 keV, 200 keV, 500 keV, 1 MeV and 2 MeV) for a standard CatPhan phantom are shown in Figure 5-8(c)-(j), respectively. The corresponding CBCT axial slices using solely kV (125kV) or MV (4MV) projections are shown in Figure 5-8(a) and (b), respectively. For notation purposes, VM energies have the unit of eV (keV or MeV).

The contrast-to-noise ratios (CNRs) of the inserts from the VM CBCTs for the range of selected energies are shown in Figure 5-9. The green and red dashed lines in each plot represent the CNR measured from the kV and MV CBCTs, respectively. The CNR values for the polymethylpentene (PMP) and low-density polyethylene (LDPE) inserts shown in Figure 5-9(b) and (c) from the VM CBCTs could be higher than those in kV CBCTs, which indicated that a lower energy is more desirable. For the Delrin insert shown in Figure 5-9(d), CNR increases as VM energy increases, which implies that a higher energy is more desirable.

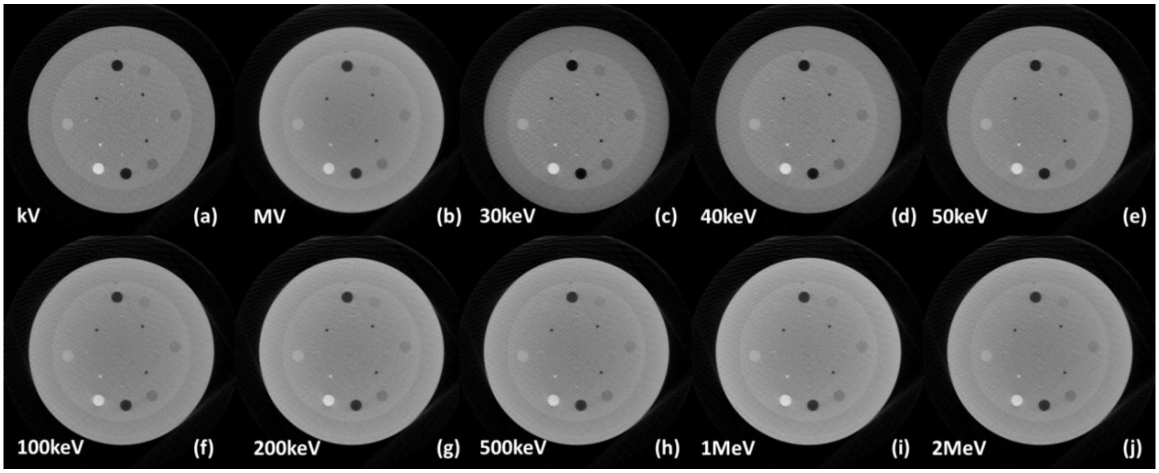

Figure 5-8 A standard CatPhan phantom axial slice reconstructed using: (a) solely kV (125kV) projections, (b) solely MV (4MV) projections, using synthesized VM projections at (c) 30keV, (d) 40keV, (e) 50keV, (f) 100keV, (g) 200keV, (h) 500keV, (i) 1MeV and (j) 2MeV.

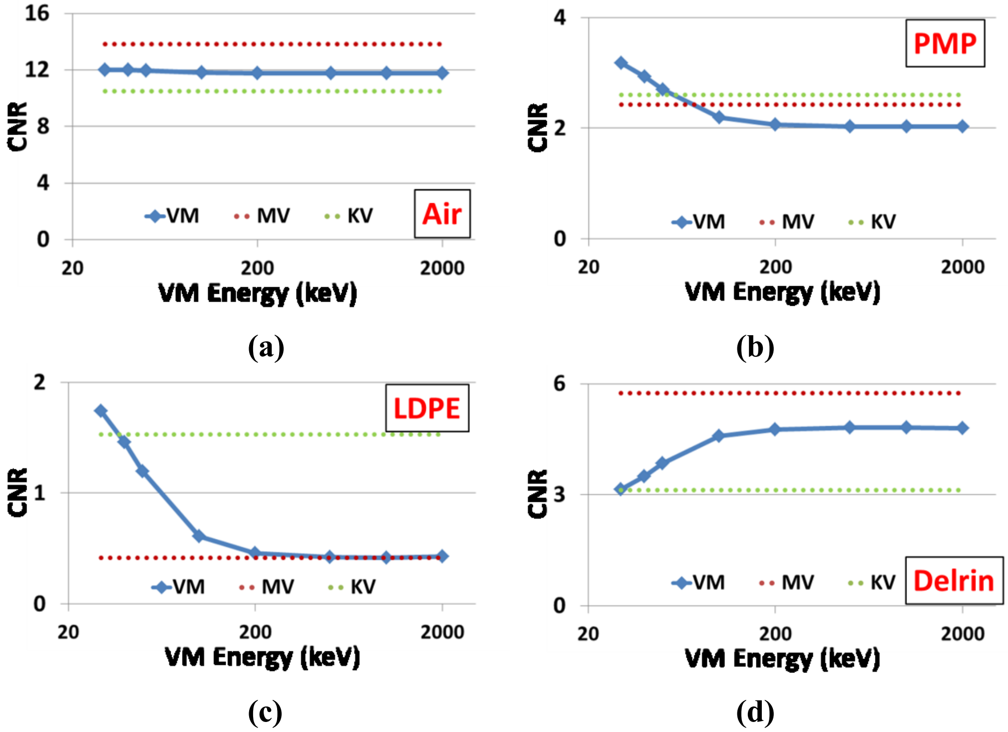

(a) **(b)**

(c) **(d)**

Figure 5-9 CNRs from VM CBCTs at different VM energies compared with those from kV and MV CBCTs for (a) air, (b) polymethylpentene (PMP), (c) low-density polyethylene (LDPE), and (d) Delrin.

5.3.2 Effect of overlap projections

Samples of the reconstructed VM CBCTs of the CatPhan at 1MeV using the conversion function based on overlap projections of 1, 5, and 10 are shown in Figure 5-10(a), (b) and (c), respectively. The table in Figure 5-10(d) shows CNRs calculated for the CatPhan inserts. Only marginal improvements of the CNR (less than 2%, except for LDPE) were observed using this specific phantom. For LDPE, it is clear that only one overlap projection would be necessary.

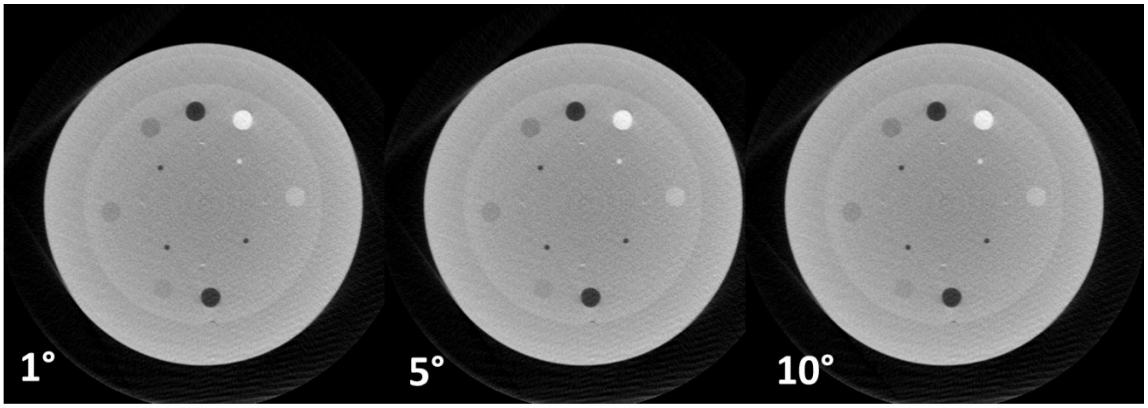

(a) (b) (c)

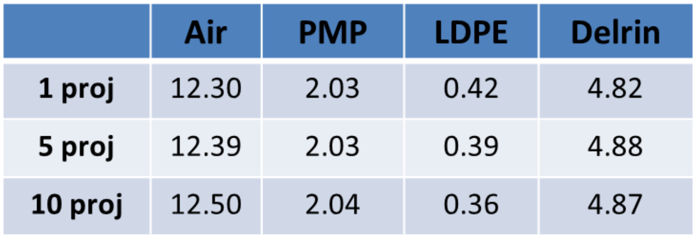

	Air	PMP	LDPE	Delrin
1 proj	12.30	2.03	0.42	4.82
5 proj	12.39	2.03	0.39	4.88
10 proj	12.50	2.04	0.36	4.87

(d)

Figure 5-10 Standard CatPhan phantom axial slices in VM CBCT created using conversion function based on (a) one, (b) five, and (c) ten overlap projections; (d) CNR results for different inserts using various numbers of projections.

5.3.3 Effect of beam orientation

Samples of the sandwiched CatPhan VM CBCT axial slices at 1MeV reconstructed with four representative starting gantry angles (30°, 120°, 210°, and 300°) are shown in Figure 5-11(a). The CNR as a function of starting angle is shown in Figure 5-11(b). It can be seen from Figure 5-11(b) that, a starting angle of 120° or 300° provides optimal CNR values for both ROI 1 and ROI 2, as shown in Figure 5-7(a). These two starting angles correspond to the orientations of solid water phantoms on both lateral sides of the CatPhan, as shown in Figure 5-7(b). With these two starting angles, lateral MV beams penetrated the phantom laterally, along the heavy attenuation directions. While for starting angles of 30° and 210°, the kV beams penetrated the phantom along the heavy attenuation direction.

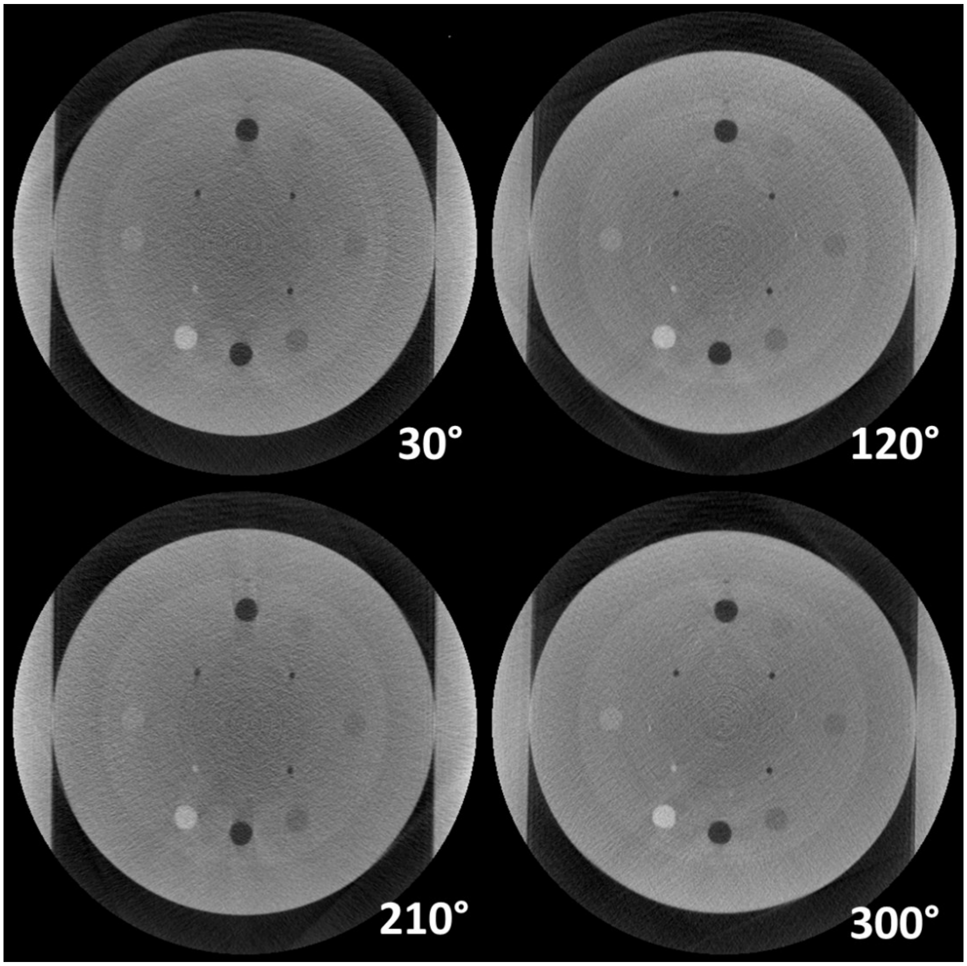

(a)

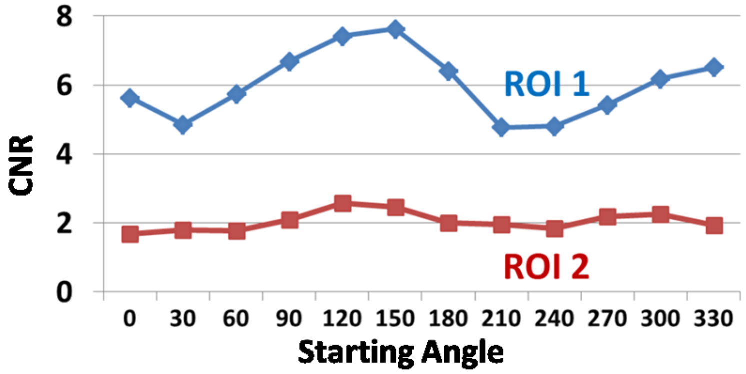

(b)

Figure 5-11 (a) CBCT of CatPhan sandwiched between two 5cm solid water phantoms laterally at different starting angles: 30°, 120°, 210° and 300°, (b) CNR as a function of starting angle for ROIs 1 and 2.

The CBCT images of the electronic density phantom with two bolt inserts using MV and kV beams are shown in Figure 5-12(a) and (b), respectively. Substantial streak artifacts are observed in the kV CBCT. VM CBCTs at 1MeV with two kV/MV beam orientation configurations are shown in Figure 5-12(c) and (d). The streak artifact is suppressed when the MV beam is oriented towards the heavy attenuation direction, as shown in Figure 5-12(d). This artifact reduction is less prominent when the kV beam is oriented toward the heavy attenuation direction, as seen in Figure 5-12(c).

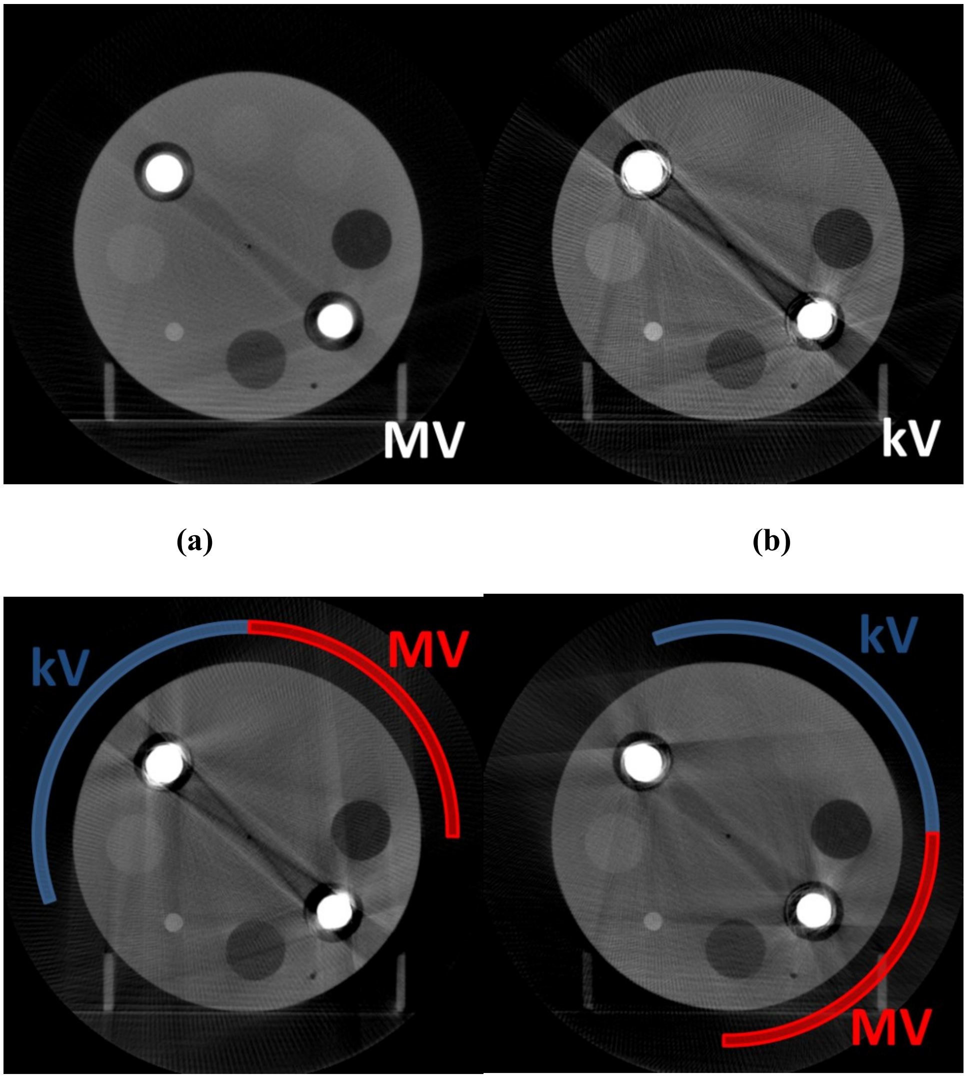

(a) (b)

(c) (d)

Figure 5-12 Electronic density phantom with two bolt inserts: CBCT with (a) MV beam, and (b) kV beam; VM CBCT with (c) kV beam along heavy attenuation direction, and (d) MV beam along heavy attenuation direction. Window: [-500 2000]

5.3.4 Effect of iterative reconstruction

The VM CBCT images at 1MeV reconstructed using the FDK method and the SART method for the CatPhan is compared in Figure 5-13. Figure 5-13(a)-(e) show VM CBCTs reconstructed with a reduced number of projections: (a) all (200 projections), (b) half (100 projections), (c) one third (67 projections), (d) one fifth (41 projections) and (e) one tenth (21 projections). Correlations of FDK and SART reconstruction using diminishing projection numbers are calculated with respect to FDK* and SART*, thus creating four curves in Figure 5-13(f), where FDK* and SART* indicate the corresponding VM CBCTs reconstructed using all 200 projections. It is clear that the correlation between FDK* and FDK images drops dramatically. The SART method is less sensitive to the discontinuities. Comparatively, the CBCTs reconstructed using the SART method is much less noisy than those reconstructed using the FDK method. The slightly blurry edge of the images is partly related with the limited projections, consistent with results seen in the previous publication[47].

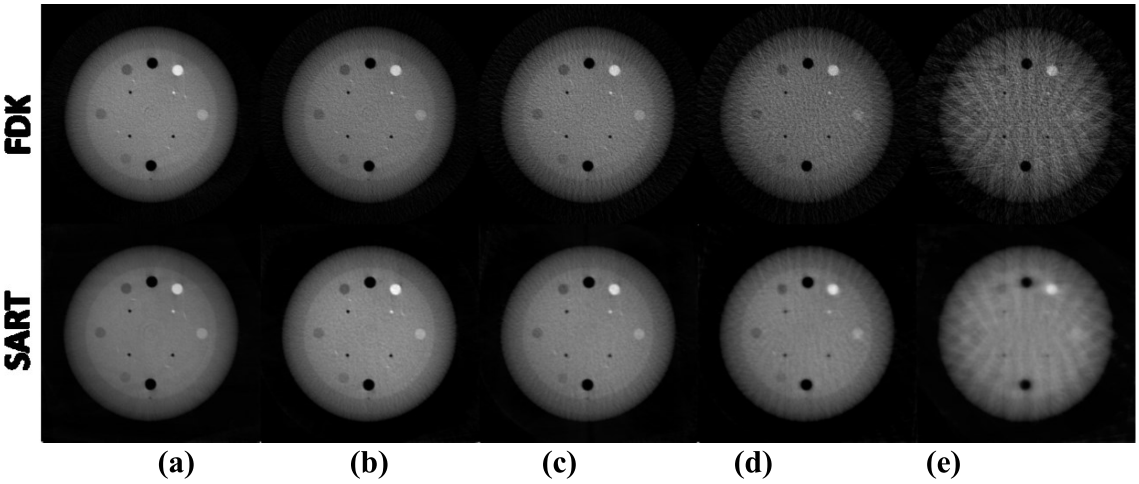

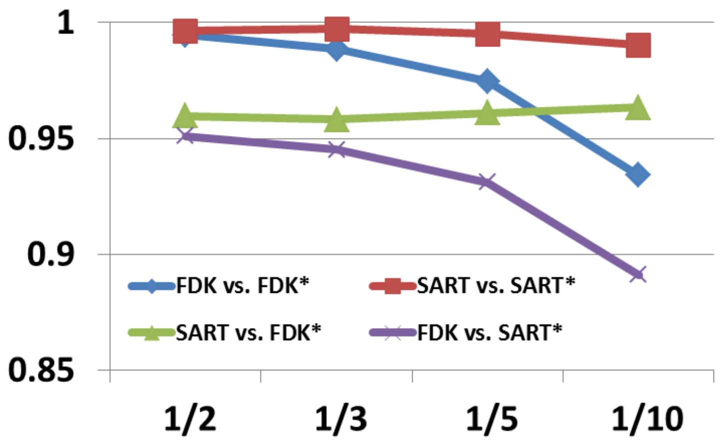

(f)

Figure 5-13 VM CBCT reconstruction using FDK and SART methods from (a) all, (b) one half, (c) one third, (d) one fifth and (e) one tenth of total projections; (f) correlation between FDK and SART results. Window: [-1000, 1000].

5.4 Discussion

The extension of the traditional dual-energy technique to kV/MV reconstruction provides a possibility to generate virtual monochromatic CBCT. Previously, no such study has been performed for kV/MV reconstruction. The dual kV/MV imaging was performed by directly converting kV and MV projections at non-overlap regions into virtual monochromatic projections covering 200°. Note that, if the two basis materials are too similar, the dual energy composition using Eqs. (5.4) becomes unstable. The linear function used to convert kV/MV projections into VM projections was only an approximation. Because of the imperfect conversion, some artifacts can still be observed in the image, especially along the directions where kV and MV projections overlap, e.g. Figure 5-12(c) and (d).

Because we used MV beams with an energy above 1.02MeV, pair production is possible. However, the effective energy of the beam is much lower than 4MeV and remains at the low end of the pair production window for water and soft tissue. Thus, the contribution of pair production in the attenuation coefficient for soft tissue is not substantial[79]. The spectrum of the MV beam is needed to quantify this contribution and this will be part of a future study.

The CNR values for low contrast objects can be improved by using different VM energies. For low density objects , PMP and LDPE, (with density of 0.83 g/cm^3 and 0.92 g/cm^3, as shown in Figure 5-9(b) and (c), respectively), a low VM energy selection is preferred. However, for high density objects, Delrin (with density of 1.41 g/cm^3, as shown in Figure 5-9(d)), a high VM energy selection is desired. This can be partially explained by their difference in electronic density. The background material has an electron density of 3.83×10^{23} e/cm^3, while the electron densities for PMP, LDPE and Delrin are 2.85×10^{23} e/cm^3, 3.16×10^{23} e/cm^3 and 4.53×10^{23} e/cm^3, respectively. The photoelectric absorption component decreases rapidly as the photon energy increases, while the Compton scatter component is a more gentle function of photon energy. Also, the photoelectric effect is highly correlated with the atomic number Z, while the Compton scatter is almost independent of Z but proportional to the electron density. When a low VM energy is selected for low electron density inserts, the photoelectric effect difference between the inserts and background is magnified, which leads to an improved CNR. For high electron density inserts, the difference in electron density magnifies the difference in Compton scatter and thus improves the CNR when the high VM energy is selected.

Table 5-1 Chemical composition, density and electron density of low contrast inserts

Material	Chemical Composition	Density (g/cm^3)	Electron Density (10^{23} e/cm^3)
LDPE	[C_2H_4]	0.92	3.16
PMP	[$C_6H_{12}(CH_2)$]	0.83	2.85
Delrin	Proprietary	1.41	4.53
Acrylic	[$C_5H_8O_2$]	1.18	3.83

The number of overlap projections used did not have a substantial effect on the image quality in terms of CNR for the phantom studied. One projection overlap could provide equivalent CNR (within 2% difference) when compared with a ten projection overlap. The biggest difference was for LDPE, which was about 15%. However, in this case, one projection overlap actually had better CNR when compared with a projection overlap of ten. Since only two parameters are needed for determining a linear fitting conversion function, the projection data can be quite redundant and thus one projection is sufficient. This will lower the number of MV projections needed and reduce the imaging dose, which comes primarily from the MV beams. However, more study will be required to recommend an imaging protocol using 91° of MV scan and 110° of kV.

In theory, when the VM technique is applied, streak artifacts which are associated with the polychromatic nature of X-ray beams should be removed. However, since a linear function was used to convert kV/MV projections into VM projections, this is only an approximation for the non-overlap gantry angles. The orientation of the MV beam was seen to have an impact on the imaging results, especially when the method was applied for metal artifact reduction. Because the attenuation coefficient for kV beams changes substantially between metal implants and the phantom, strong streak artifacts are observed in Figure 5-12(b). The attenuation coefficient for MV beams has a much smaller change, and very limited streak artifacts can be seen in Figure 5-12(a). Photon starvation is usually a major cause of streak artifacts induced by metal implants. Therefore, when the MV beam is oriented along the direction of heavy attenuation in the object, most photons can still penetrate the implants and the streak artifacts are substantially suppressed. The same logic also applies to non-round objects, as illustrated in Figure 5-11(b). A typical patient at the treatment position is usually thicker along the lateral direction and thinner along the anterior-posterior direction. Thus, it can be beneficiary to orient the beam in such an angular set-up to optimize the image results.

A radiographic mode was used in this study for MV image acquisition in TrueBeam Developer Mode, which requires at least 3MU delivered per projection. It apparently is not feasible for clinical patient application. Imaging dose for a patient undergoing radiation therapy could be a concern because the imaging volume is substantially larger than the treatment target volume. Thus, it is necessary to minimize the imaging dose even to cancer patients undergoing radiation therapy. However, as sub-monitor unit (MU) imaging develops and becomes available for clinical use, the technique could be implemented with reasonable low-dose MV beams. Furthermore, since less than half of the scan is acquired with the kV beam, the technique can reduce the imaging dose substantially compared with a complete MV CBCT while retaining some key benefits of MV imaging. Further study is warranted to understand how many MV projections and how many MUs are needed for image acquisition in order to generate CBCTs with acceptable image quality for localization purposes.

The projections from the two imaging chains, kV and MV imagers, were mapped into one coordinate system during reconstruction. Any possible misalignment of the two isocenters and tilt of detector could lead to imaging artifacts. However, proper vendor calibrations (IsoCal calibration from Varian) could minimize the artifacts resulting from the mechanical instability.

Accurate VM projection synthesis at the overlap angles requires that the imaging objects remain stationary. In our set-up, kV and MV Projections at the overlap angles are acquired sequentially. If applied in the clinics, this sequential acquisition translates to a time gap of approximately 15 seconds (90° gap with 6°/s gantry rotational speed). Patient movement during this time gap may cause artifacts in the VM synthesis at overlap angles.

5.5 Conclusions

A novel aggregate technique was proposed to generate VM CBCTs from kV/MV projections. The technique provides the potential to improve CNR depending on the selected VM energy. To achieve the optimal image quality for the dual kV/MV imaging, the best orientation of kV/MV beams is through the heavy attenuation direction for MV beams and through the light attenuation direction for kV beams.

6. Concluding Remarks

Before investigation of the imaging capabilities of a bench-top DCBCT system using two kV-sources, the system performance was firstly characterized in terms of its uniformity, contrast, spatial resolution, noise power spectrum, and CT number linearity. Compared to single CBCT, the DCBCT presented: 1) a decrease in uniformity by 1.9% in axial view and 1.1% in the longitudinal view, as averaged over four energies (80, 100, 125 and 150 kVp); 2) comparable or slightly better contrast to noise ratio (CNR) for low-contrast objects and comparable contrast for high-contrast objects; 3) comparable spatial resolution; 4) comparable CT number linearity with $R^2 \geq 0.99$ for all four tested energies; and 5) lower noise power spectrum in magnitude. DCBCT sample images of the skull phantom and the ham demonstrated both high-contrast resolution and good soft-tissue contrast. These data provide confidence for researchers to perform more advanced imaging tasks on the platform.

To investigate the 4D imaging capabilities of the DCBCT system, motion phantom studies were conducted to validate the efficiencies by comparing 4D images generated from 4D-DCBCT and 4D-CBCT using different breathing profiles. The DCBCT system benefited the temporal resolution in two ways: 1) short acquisition time; and 2) simultaneous acquisition between two detectors. For one extreme example using the irregular sinusoidal wave, 4D-DCBCT had generated a significantly less motionblurred image. For patient-derived breathing profiles, this reduction in motion blur is less significant.

To implement dual kV energy imaging on a CBCT platform, we acquired 80kVp projections and 150 kVp projections, with an additional 0.8 mm tin filtration. The VM technique was shown to be effective in the metal artifact and beam hardening reduction and the LM technique was shown to improve CNR levels when compared with equivalent-dose single-energy CBCTs.

For application of the dual-energy technique in the kilovoltage (kV) and megavoltage (MV) range, we acquired both MV projections (from gantry angle of 0° to 100°) and kV projections (90° to 200°) with the current orthogonal kV/MV imaging hardware equipped on modern linear accelerators, as gantry rotated a total of 110°. Selection of the VM energy can provide comparable or even better CNR results when compared with kV or MV CBCT. It was also evident that the optimal CBCT image quality was achieved when MV beams penetrated through the heavy attenuation direction of the object.

Some possible future works may include utilizing DCBCT system for dual digital tomosynthesis (DTS) tasks. In conventional DTS, out-of-plane blur is always observed, due to undersampling during acquisition[80], which may degrade the localization accuracy along the out-of-plane direction. With the DCBCT system, however, the orthogonal depth information along the out-of-plane direction for one detector can be acquired by the other detector at the orthogonal direction. The information obtained from the dual DTS may be sufficient for localization purposes in radiation therapy because the two X-ray tube/detector sets can provide complementary information. Moreover, dual DTS reduces the scan time and imaging dose when compared with a CBCT scan.

In conclusion, dual cone-beam/dual energy imaging techniques provides flexibilities for researchers and potential clinical practice. These techniques can be utilized towards motion management, artifact reduction, CNR improvement, and more generally can be applied towards image quality enhancement.

References

1. Siegel, R., D. Naishadham, and A. Jemal, Cancer statistics, 2013. CA: A Cancer Journal for Clinicians, 2013. **63**(1): p. 11-30.

2. Jaffray, D.A., et al., Flat-panel cone-beam computed tomography for image-guided radiation therapy. International Journal of Radiation Oncology, Biology, Physics, 2002. **53**(5): p. 1337-49.

3. Xing, L., et al., Overview of image-guided radiation therapy. Medical Dosimetry, 2006. **31**(2): p. 91-112.

4. Dawson, L.A. and D.A. Jaffray, Advances in image-guided radiation therapy. Journal of clinical oncology, 2007. **25**(8): p. 938-946.

5. Bourland, J.D., Image-guided Radiation Therapy. 2012: CRC PressI Llc.

6. Oldham, M., et al., Cone-beam-CT guided radiation therapy: A model for on-line application. Radiotherapy and Oncology, 2005. **75**(3): p. 271-8.

7. Sonke, J.J., et al., Respiratory correlated cone beam CT. Medical Physics, 2005. **32**(4): p. 1176-86.

8. Oelfke, U., et al., Linac-integrated kV-cone beam CT: technical features and first applications. Medical Dosimetry, 2006. **31**(1): p. 62-70.

9. Chang, J., et al., Accuracy and feasibility of cone-beam computed tomography for stereotactic radiosurgery setup. Medical Physics, 2007. **34**(6): p. 2077-84.

10. Letourneau, D., et al., Cone-beam-CT guided radiation therapy: technical implementation. Radiotherapy and Oncology, 2005. **75**(3): p. 279-286.

11. Flohr, T., et al., First performance evaluation of a dual-source CT (DSCT) system. European Radiology, 2006. **16**(2): p. 256-268.

12. Graser, A., et al., Dual energy CT: preliminary observations and potential clinical applications in the abdomen. European Radiology, 2009. **19**(1): p. 13-23.

13. Johnson, T., et al., Material differentiation by dual energy CT: initial experience. European Radiology, 2007. **17**(6): p. 1510-1517.

14. Foster, R., D. Pistenmaa, and T. Solberg, A comparison of radiographic techniques and electromagnetic transponders for localization of the prostate. Radiation Oncology, 2012. **7**(1): p. 101.

15. Rietzel, E., et al., Four-dimensional image-based treatment planning: Target volume segmentation and dose calculation in the presence of respiratory motion. International Journal of Radiation Oncology, Biology and Physics, 2005. **61**(5).

16. Sonke, J.-J., et al., Respiratory correlated cone beam CT. Medical physics, 2005. **32**: p. 1176.

17. Dietrich, L., et al., Linac-integrated 4D cone beam CT: first experimental results. Physics in Medicine and Biology, 2006. **51**(11): p. 2939-52.

18. Li, T., et al., Four-dimensional cone-beam computed tomography using an on-board imager. Medical physics, 2006. **33**: p. 3825.

19. Lu, J., et al., Four-dimensional cone beam CT with adaptive gantry rotation and adaptive data sampling. Medical physics, 2007. **34**: p. 3520.

20. Alvarez, R. and E. Seppi, A Comparison of Noise and Dose in Conventional and Energy Selective Computed Tomography. Nuclear Science, IEEE Transactions on, 1979. **26**(2): p. 2853-2856.

21. Kalender, W.A., et al., Evaluation of a prototype dual-energy computed tomographic apparatus. I. Phantom studies. Medical Physics, 1986. **13**(3): p. 334-9.

22. Schwarz, F., et al., Dual-energy CT of the heart--Principles and protocols. European Journal of Radiology, 2008. **68**(3): p. 423-433.

23. Takahashi, N., et al., Dual-energy CT iodine-subtraction virtual unenhanced technique to detect urinary stones in an iodine-filled collecting system: a phantom study. AJR. American Journal of Roentgenology, 2008. **190**(5): p. 1169-73.

24. Chae, E.J., et al., Clinical utility of dual-energy CT in the evaluation of solitary pulmonary nodules: initial experience. Radiology, 2008. **249**(2): p. 671-81.

25. Tacelli, N., et al., Dual-source chest CT angiography with high temporal resolution and high pitch modes: evaluation of image quality in 140 patients. European Radiology, 2009.

26. Cho, S., et al. Dual-energy cone-beam micro-CT for animal imaging: preliminary study. 2007. SPIE.

27. Granton, P.V., et al., Implementation of dual- and triple-energy cone-beam micro-CT for postreconstruction material decomposition. Medical Physics, 2008. **35**(11): p. 5030-42.

28. Min, J., et al. Low-dose dual-energy cone-beam CT using a total-variation minimization algorithm. 2011. SPIE.

29. Orth, R.C., M.J. Wallace, and M.D. Kuo, C-arm Cone-beam CT: General Principles and Technical Considerations for Use in Interventional Radiology. Journal of Vascular and Interventional Radiology, 2009. **20**(7, Supplement 1): p. S538-S544.

30. Gupta, R., et al., Ultra-high resolution flat-panel volume CT: fundamental principles, design architecture, and system characterization. European Radiology, 2006. **16**(6): p. 1191-1205.

31. Farman, T.T., et al., Effects of scintillator on the detective quantum efficiency (DQE) of a digital imaging system. Oral Surgery, Oral Medicine, Oral Pathology, Oral Radiology, and Endodontology, 2006. **101**(2): p. 219-223.

32. Liu, X., et al., Quantitative imaging of element composition and mass fraction using dual-energy CT: three-material decomposition. Medical Physics, 2009. **36**(5): p. 1602-9.

33. Sonke, J.-J., et al., Frameless stereotactic body radiotherapy for lung cancer using four-dimensional cone beam CT guidance. International journal of radiation oncology, biology, physics, 2009. **74**(2): p. 567-574.

34. Pang, G., et al., Imaging of 1.0-mm-diameter radiopaque markers with megavoltage X-rays: an improved online imaging system. International Journal of Radiation Oncology*Biology*Physics, 2002. **52**(2): p. 532-537.

35. Meeks, S.L., et al., Performance characterization of megavoltage computed tomography imaging on a helical tomotherapy unit. Medical Physics, 2005. **32**(8): p. 2673-2681.

36. Morin, O., et al., Megavoltage cone-beam CT: System description and clinical applications. Medical Dosimetry, 2006. **31**(1): p. 51-61.

37. Forthmann, P., M. Grass, and R. Proksa, Adaptive two-pass cone-beam artifact correction using a FOV-preserving two-source geometry: A simulation study. Medical Physics, 2009. **36**: p. 4440.

38. Jaffray, D.A. and J.H. Siewerdsen, Cone-beam computed tomography with a flat-panel imager: initial performance characterization. Medical Physics, 2000. **27**(6): p. 1311-23.

39. Dietrich, L., et al., Linac-integrated 4D cone beam CT: first experimental results. Physics in medicine and biology, 2006. **51**(11): p. 2939.

40. W. Giles, J.B., H. Li, F. Yin, Measurement-Based Cross-Scatter Correction in Dual Detector Cone-Beam CT. 2011 Joint AAPM/COMP Meeting, 2011.

41. Siewerdsen, J.H. and D.A. Jaffray, Optimization of x-ray imaging geometry (with specific application to flat-panel cone-beam computed tomography). Medical Physics, 2000. **27**(8): p. 1903-1914.

42. Johnston, S.M., G.A. Johnson, and C.T. Badea, Geometric calibration for a dual tube/detector micro-CT system. Medical Physics, 2008. **35**(5): p. 1820-9.

43. Yang, K., et al., A geometric calibration method for cone beam CT systems. Medical Physics, 2006. **33**(6): p. 1695-706.

44. Feldkamp, L.A., L.C. Davis, and J.W. Kress, Practical cone-beam algorithm. J. Opt. Soc. Am. A, 1984. **1**(6): p. 612-619.

45. Siewerdsen, J.H., I.A. Cunningham, and D.A. Jaffray, A framework for noise-power spectrum analysis of multidimensional images. Medical Physics, 2002. **29**(11): p. 2655-71.

46. Boedeker, K.L., V.N. Cooper, and M.F. McNitt-Gray, Application of the noise power spectrum in modern diagnostic MDCT: part I. Measurement of noise power spectra and noise equivalent quanta. Physics in Medicine and Biology, 2007. **52**(14): p. 4027.

47. Yin, F.-F., H. Guan, and W. Lu, A technique for on-board CT reconstruction using both kilovoltage and megavoltage beam projections for 3D treatment verification. Medical Physics, 2005. **32**(9): p. 2819-2826.

48. Zhang, J. and F.-F. Yin, Minimizing image noise in on-board CT reconstruction using both kilovoltage and megavoltage beam projections. Medical Physics, 2007. **34**(9): p. 3665-3673.

49. Blessing, M., et al., Breath-Hold Target Localization With Simultaneous Kilovoltage/Megavoltage Cone-Beam Computed Tomography and Fast Reconstruction. International Journal of Radiation Oncology*Biology*Physics, 2010. **78**(4): p. 1219-1226.

50. Wertz, H., et al., Fast kilovoltage/megavoltage (kVMV) breathhold cone-beam CT for image-guided radiotherapy of lung cancer. Physics in Medicine and Biology, 2010. **55**(15): p. 4203.

51. Li, T., et al., Four-dimensional cone-beam computed tomography using an on-board imager. Medical Physics, 2006. **33**(10): p. 3825-33.

52. Purdie, T.G., et al., Respiration correlated cone-beam computed tomography and 4DCT for evaluating target motion in Stereotactic Lung Radiation Therapy. Acta Oncologica, 2006. **45**(7): p. 915-922.

53. Lu, J., et al., Four-dimensional cone beam CT with adaptive gantry rotation and adaptive data sampling. Medical Physics, 2007. **34**(9): p. 3520-9.

54. Maurer, J., et al., On-board four-dimensional digital tomosynthesis: First experimental results. Medical physics, 2008. **35**: p. 3574.

55. Kalender, W.A., R. Hebel, and J. Ebersberger, Reduction of CT artifacts caused by metallic implants. Radiology, 1987. **164**(2): p. 576-7.

56. Yazdi, M., L. Gingras, and L. Beaulieu, An adaptive approach to metal artifact reduction in helical computed tomography for radiation therapy treatment planning: experimental and clinical studies. International Journal of Radiation Oncology, Biology, Physics, 2005. **62**(4): p. 1224-31.

57. Nuyts, J., et al., Iterative reconstruction for helical CT: a simulation study. Physics in Medicine and Biology, 1998. **43**(4): p. 729-37.

58. Roeske, J.C., et al., Reduction of computed tomography metal artifacts due to the Fletcher-Suit applicator in gynecology patients receiving intracavitary brachytherapy. Brachytherapy, 2003. **2**(4): p. 207-14.

59. Zhang, Y., et al., Reducing metal artifacts in cone-beam CT images by preprocessing projection data. International Journal of Radiation Oncology, Biology, Physics, 2007. **67**(3): p. 924-32.

60. Schulze, R.K., D. Berndt, and B. d'Hoedt, On cone-beam computed tomography artifacts induced by titanium implants. Clinical Oral Implants Research, 2010. **21**(1): p. 100-7.

61. Bamberg, F., et al., Metal artifact reduction by dual energy computed tomography using monoenergetic extrapolation. European Radiology, 2011. **21**(7): p. 1424-1429.

62. Alvarez, R.E. and A. Macovski, Energy-selective reconstructions in X-ray computerized tomography. Physics in Medicine and Biology, 1976. **21**(5): p. 733-44.

63. Matsumoto, K., et al., Virtual Monochromatic Spectral Imaging with Fast Kilovoltage Switching: Improved Image Quality as Compared with That Obtained with Conventional 120-kVp CT. Radiology, 2011. **259**(1): p. 257-262.

64. Zou, Y. and M.D. Silver, Analysis of fast kV-switching in dual energy CT using a pre-reconstruction decomposition technique. Vol. 6913. 2008: SPIE. 691313.

65. Cardinal, H.N. and A. Fenster, An accurate method for direct dual-energy calibration and decomposition. Medical Physics, 1990. **17**(3): p. 327-41.

66. Lin, X.Z., et al., High-Definition CT Gemstone Spectral Imaging of the Brain: Initial Results of Selecting Optimal Monochromatic Image for Beam-Hardening Artifacts and Image Noise Reduction. Journal of Computer Assisted Tomography, 2011. **35**(2): p. 294-297 10.1097/RCT.0b013e3182058d5c.

67. Wu, X., et al., Monochromatic CT image representation via fast switching dual kVp. Vol. 7258. 2009: SPIE. 725845.

68. Yu, L., et al., Image quality optimization and evaluation of linearly mixed images in dual-source, dual-energy CT. Medical Physics, 2009. **36**(3): p. 1019-1024.

69. Hui, X., et al. Metal artifact reduction in dual energy CT by sinogram segmentation based on active contour model and TV inpainting. in Nuclear Science Symposium Conference Record (NSS/MIC), 2009 IEEE. 2009.

70. Graser, A., et al., Dual Energy CT Characterization of Urinary Calculi: Initial In Vitro and Clinical Experience. Investigative Radiology, 2008. **43**(2): p. 112-119 10.1097/RLI.0b013e318157a144.

71. Johnson, T.R., et al., Material differentiation by dual energy CT: initial experience. European Radiology, 2007. **17**(6): p. 1510-7.

72. Kalender, W.A., E. Klotz, and L. Kostaridou, An algorithm for noise suppression in dual energy CT material density images. Medical Imaging, IEEE Transactions on, 1988. **7**(3): p. 218-224.

73. Yu, L., et al., Virtual monochromatic imaging in dual-source dual-energy CT: Radiation dose and image quality. Medical Physics, 2011. **38**(12): p. 6371-6379.

74. Heaven, T.J., et al., Density measurements of dentin by dual-energy radiography. Oral Surgery, Oral Medicine, Oral Pathology, Oral Radiology, and Endodontology, 2010. **109**(4): p. 604-614.

75. Ducote, J.L. and S. Molloi, Quantification of breast density with dual energy mammography: An experimental feasibility study. Medical Physics, 2010. **37**(2): p. 793-801.

76. Magnusson, M., et al., Iterative Reconstruction for Quantitative Tissue Decomposition in Dual-Energy CT Image Analysis, A. Heyden and F. Kahl, Editors. 2011, Springer Berlin / Heidelberg. p. 479-488.

77. Lehmann, L.A., et al., Generalized image combinations in dual KVP digital radiography. Medical Physics, 1981. **8**(5): p. 659-667.

78. Wang, G. and M. Jiang, Ordered-subset simultaneous algebraic reconstruction techniques (OS-SART). Journal of X-ray Science and Technology, 2004. **12**(3): p. 169-178.

79. Khan, F.M. and F. Khan, The physics of radiation therapy. Vol. 4. 2003: Lippincott Williams & Wilkins Philadelphia.

80. Dobbins, J.T., 3rd and D.J. Godfrey, Digital x-ray tomosynthesis: current state of the art and clinical potential. Physics in Medicine and Biology, 2003. **48**(19): p. R65-106.

Biography

Name:

Hao Li

Place of Birth:

Nanjing, Jiangsu, China

Education:

Duke University, Durham NC, USA 2008 - 2013
Ph.D. in Medical Physics

Tsinghua University, Beijing, China 2002 - 2008
Department of Biomedical Engineering, School of Medicine
M.S. in Biomedical Engineering
B.S. in Biomedical Engineering